View metadata, citation and similar papers at core.ac.uk

brought to you by CORE

provided by NASA Technical Reports S

This article was downloaded by: [Texas A&M University Libraries and your student fees]
On: 22 December 2011, At: 08:16
Publisher: Taylor & Francis
Informa Ltd Registered in England and Wales Registered Number: 1072954 Registered office: Mortimer House, 37-41 Mortimer Street, London W1T 3JH, UK

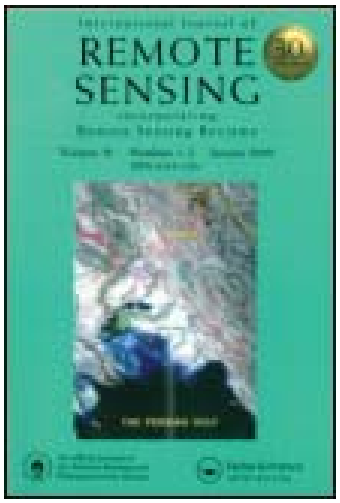

International Journal of Remote Sensing

Publication details, including instructions for authors and subscription information:
http://www.tandfonline.com/loi/tres20

Determination of ice cloud models using MODIS and MISR data

Yu Xie [a] , Ping Yang [a] , George W. Kattawar [b] , Patrick Minnis [c] , Yongxiang Hu [c] & Dong L. Wu [d]

[a] Department of Atmospheric Sciences, Texas A&M University, College Station, TX, 77843, USA

[b] Department of Physics & Astronomy, Texas A&M University, College Station, TX, 77843, USA

[c] NASA Langley Research Center, Hampton, VA, 23681, USA

[d] Jet Propulsion Laboratory, Pasadena, CA, 91109, USA

Available online: 22 Dec 2011

To cite this article: Yu Xie, Ping Yang, George W. Kattawar, Patrick Minnis, Yongxiang Hu & Dong L. Wu (2012): Determination of ice cloud models using MODIS and MISR data, International Journal of Remote Sensing, 33:13, 4219-4253

To link to this article: http://dx.doi.org/10.1080/01431161.2011.642323

PLEASE SCROLL DOWN FOR ARTICLE

Full terms and conditions of use: http://www.tandfonline.com/page/terms-and-conditions

This article may be used for research, teaching, and private study purposes. Any substantial or systematic reproduction, redistribution, reselling, loan, sub-licensing, systematic supply, or distribution in any form to anyone is expressly forbidden.

The publisher does not give any warranty express or implied or make any representation that the contents will be complete or accurate or up to date. The accuracy of any instructions, formulae, and drug doses should be independently verified with primary sources. The publisher shall not be liable for any loss, actions, claims, proceedings, demand, or costs or damages whatsoever or howsoever caused arising directly or indirectly in connection with or arising out of the use of this material.

International Journal of Remote Sensing
Vol. 33, No. 13, 10 July 2012, 4219–4253

Taylor & Francis
Taylor & Francis Group

Determination of ice cloud models using MODIS and MISR data

YU XIE*†, PING YANG†, GEORGE W. KATTAWAR‡, PATRICK MINNIS§, YONGXIANG HU§ and DONG L. WU¶**

†Department of Atmospheric Sciences, Texas A&M University, College Station, TX 77843, USA
‡Department of Physics & Astronomy, Texas A&M University, College Station, TX 77843, USA
§NASA Langley Research Center, Hampton, VA 23681, USA
¶Jet Propulsion Laboratory, Pasadena, CA 91109, USA

(*Received 21 December 2010; in final form 13 October 2011*)

Representation of ice clouds in radiative transfer simulations is subject to uncertainties associated with the shapes and sizes of ice crystals within cirrus clouds. In this study, we examined several ice cloud models consisting of smooth, roughened, homogeneous and inhomogeneous hexagonal ice crystals with various aspect ratios. The sensitivity of the bulk scattering properties and solar reflectances of cirrus clouds to specific ice cloud models is investigated using the improved geometric optics method (IGOM) and the discrete ordinates radiative transfer (DISORT) model. The ice crystal habit fractions in the ice cloud model may significantly affect the simulations of cloud reflectances. A new algorithm was developed to help determine an appropriate ice cloud model for application to the satellite-based retrieval of ice cloud properties. The ice cloud particle size retrieved from Moderate Resolution Imaging Spectroradiometer (MODIS) data, collocated with Multi-angle Imaging Spectroradiometer (MISR) observations, is used to infer the optical thicknesses of ice clouds for nine MISR viewing angles. The relative differences between view-dependent cloud optical thickness and the averaged value over the nine MISR viewing angles can vary from −0.5 to 0.5 and are used to evaluate the ice cloud models. In the case for 2 July 2009, the ice cloud model with mixed ice crystal habits is the best fit to the observations (the root mean square (RMS) error of cloud optical thickness reaches 0.365). This ice cloud model also produces consistent cloud property retrievals for the nine MISR viewing configurations within the measurement uncertainties.

Downloaded by [Texas A&M University Libraries and your student fees] at 08:16 22 December 2011

1. Introduction

Field campaigns such as the First International Satellite Cloud Climatology Project (ISCCP) Regional Experiments (FIRE) (Starr 1987), Tropical Rainfall Measurement Mission (TRMM) (Silva Dias *et al.* 2002, Yuter *et al.* 2005) and Cirrus Regional Study of Tropical Anvils and Cirrus Layers – Florida Area Cirrus Experiment (CRYSTAL-FACE) (Jensen *et al.* 2004) have demonstrated that ice crystals within cirrus clouds are normally defective and irregular in shape (Heymsfield *et al.* 1990, Arnott *et al.*

*Corresponding author. Email: xieyupku@tamu.edu
**Present address: NASA/Goddard Space Flight Center, Breenbelt, MD 20771, USA.

International Journal of Remote Sensing
ISSN 0143-1161 print/ISSN 1366-5901 online © 2012 Taylor & Francis
http://www.tandf.co.uk/journals
http://dx.doi.org/10.1080/01431161.2011.642323

Downloaded by [Texas A&M University Libraries and your student fees] at 08:16 22 December 2011

1994, Korolev *et al.* 1999, Heymsfield *et al.* 2002, Nasiri *et al.* 2002, Heymsfield and Miloshevich 2003, Baumgardner *et al.* 2005, Chepfer *et al.* 2005). The great natural variability of cloud ice crystal habits causes large uncertainties in the computation of the transfer of electromagnetic radiation involving cirrus clouds and has drawn a great deal of attention, as evidenced by the large volume of research devoted to the topic (Macke 1993, Yang and Liou 1998, Masuda *et al.* 2002, Mcfarquhar *et al.* 2002, Baran *et al.* 2005, Lawless *et al.* 2006, Wendisch *et al.* 2007, Yang and Fu 2009). To improve the treatment of the bulk radiative properties of ice clouds in various remote-sensing and climate modelling applications, the applied optics community needs to first fully understand and provide accurate scattering and absorption characteristics of a monodispersed ensemble of ice crystals, since this represents the simplest arrangement of ice crystals.

A fundamental hindrance to simulating the light scattering of ice crystals is the difficulty in obtaining realistic representations of natural ice crystals arising primarily from their complex particle shapes. Individual ice crystal structure is affected by a number of factors including the temperature, humidity and pressure at which ice crystals form (Kobayashi 1961, Kajikawa and Heymsfield 1989, Bailey and Hallett 2004, Baker and Lawson 2006, Lawson *et al.* 2006). Several physical processes can further modify the appearance of ice crystals during their vertical motion within clouds. Ice crystals can become unidentifiable aggregates when they fall through the cloud layer and collide with supercooled water droplets or other ice crystals. Additionally, the surfaces of ice crystals are generally not perfectly smooth because of collisions, coalescence and other fragmenting processes. Although the exact mechanism for forming various ice crystal habits is not well understood, hexagonal columns (HCs) and plates (HPs) are known to be the important habits of ice crystals commonly found in cirrus clouds. This has been confirmed by both *in situ* measurements of cirrus clouds and the optical phenomena that 22° halos, caused by sunlight refracted by hexagonal ice crystals, are usually seen when the sky is overspread with thin cirrus clouds (Coleman and Liou 1981, Sassen *et al.* 1994).

Based on the ice crystal habit and size distributions obtained from *in situ* measurements and the work conducted to simulate light scattering by nonspherical particles (Cai and Liou 1982, Takano and Liou 1995, Macke and Mishchenko 1996, Yang and Liou 1996a,b, 1997, 1998, Baran *et al.* 2001b), ice crystals with hexagonal structures are often assumed in the retrievals of cirrus cloud microphysical and optical properties from satellite observations (Minnis *et al.* 1993, King *et al.* 1996, Minnis *et al.* 1998, Chepfer *et al.* 2001, King *et al.* 2004, Minnis *et al.* 2004, Li *et al.* 2005, Minnis *et al.* 2011). A mixture of more complicated ice crystal shapes has also been suggested for ice cloud optical models (Baum *et al.* 2000, 2005a,b, 2007, Xie *et al.* 2011). The quality of the satellite retrieval depends on the accuracies of the scattering properties used to represent natural hexagonal ice crystals in cirrus clouds and on the resulting simulated cirrus cloud solar reflectances.

Efforts have been made to study the sensitivity of certain morphological parameters of hexagonal ice crystals to the single-scattering properties of ice crystals. Yang and Liou (1998) modelled the ice crystal surface roughness by using the slopes of the facets to define the degree of surface roughness. The radiation scattering by the rough-surfaced hexagonal ice crystals has been investigated using both rigorous and simplified algorithms based on the ray-tracing technique (Yang *et al.* 2008b). The primary effect of ice crystal surface roughness, relative to using smooth crystals, is to increase the solar reflectances in visible regions at most angles and to decrease the

Downloaded by [Texas A&M University Libraries and your student fees] at 08:16 22 December 2011

retrieved ice cloud optical thicknesses (Yang *et al.* 2008a). Xie *et al.* (2009) investigated the scattering properties of inhomogeneous ice crystals based on observations, in which atmospheric ice crystals were collected near the surface and studied with a binocular microscope (Tape 1994). Inhomogeneous ice crystals, containing spherical or spheroidal air bubbles, were confirmed to have the effect of reducing the ice cloud optical thicknesses when they were used in the satellite-based retrieval of ice cloud properties. In addition, air bubbles within ice crystals may substantially reduce the ice crystal volumes and affect the retrieval of ice cloud particle sizes.

Quantifying the morphological parameters (i.e. degrees of ice crystal surface roughness and inhomogeneity) and habit distributions of the ice crystals used in the operational retrieval of cloud properties would help minimize the effect of the spatial and temporal limitations of the *in situ* and surface observations of atmospheric ice crystals. In other words, a robust algorithm is needed to quickly and accurately find the most appropriate ice crystal configurations to minimize the uncertainties introduced by the use of any particular ice cloud model. Doutriaux-Boucher *et al.* (2000) derived ice cloud optical thicknesses based on the Polarization and Directionality of the Earth's Reflectances (POLDER) observations of radiances in 14 different viewing directions. Cloud spherical albedos were computed using the retrieved optical thicknesses over 'super-pixels' consisting of 9×9 elementary pixels, each of which corresponds to a spatial resolution of approximately 60 km $\times$ 60 km. The error caused by the use of ice crystal habits and their scattering properties was inferred through the departure of the spherical albedos derived from their averaged values in conjunction with the 14 view angles. This algorithm was followed by studies aimed at improving the scattering properties of cirrus clouds (Labonnote *et al.* 2001, Baran and Labonnote 2006) or retrieving ice crystal habits (Baran *et al.* 2001a, Chepfer *et al.* 2001, 2002, Sun *et al.* 2006) using POLDER multi-angle radiance measurements. McFarlane *et al.* (2005) developed a method for retrieving cloud thermodynamic phase and ice crystal habit using Multi-angle Imaging Spectroradiometer (MISR) and Moderate Resolution Imaging Spectroradiometer (MODIS) data. They assessed the accuracy of ice crystal habits by studying the relative deviation of the computed cloud reflectances and those measured by nine MISR cameras and averaged over a 10 km $\times$ 10 km box at the Atmospheric Radiation Measurement (ARM) Southern Great Plains (SGP) site. The retrieval of ice crystal habits was reasonably consistent with *in situ* observations of cirrus clouds.

The differences in retrieved cloud optical properties caused by using measurements taken at different satellite viewing directions can arise from other factors besides ice cloud habits. Theoretical studies (Davies 1984, Loeb and Davies 1997, Loeb and Coakley 1998, Iwabuchi and Hayasaka 2002) have indicated that the horizontal inhomogeneity of clouds or the 3D radiative effect may lead 1D retrievals to under- or overestimate cloud reflectances and optical thicknesses due to cloud-side shadowing or illumination. However, because of its complexity, this effect has typically been ignored in current operational retrieval of cloud properties. Moreover, the biases in cloud property retrievals introduced from viewing geometries can be partially eliminated when the results are averaged over several pixels (Oreopoulos and Davies 1998, Kato and Marshak 2009). Thus, the improvement of pixel-by-pixel retrievals of cloud properties is more meaningful if the errors are investigated using similar spatial resolutions.

In this study, we develop an ice cloud reflectance model using simple, but appropriate, ice crystal habit and size distributions to minimize directional reflectance uncertainties employing matched data from the MODIS and MISR on board the

National Aeronautics and Space Administration's (NASA's) Terra spacecraft. Given all of the uncertainties of the operationally retrieved ice cloud properties, the resulting ice cloud model exhibits excellent consistency with the measurements from the nine MISR views.

In §2, we introduce the study of ice crystal habits and their sensitivity to the scattering properties and solar reflectances of cirrus clouds. In §3, we describe the MODIS and MISR data used in the retrieval of ice cloud properties and develop a methodology to determine an optimal ice cloud model for routine retrieval of ice cloud properties using reflected solar radiation. In §4, we analyse the potential errors in retrieved ice cloud optical thicknesses in a case in which MODIS data are not employed in the retrieval. In §5, the errors caused by ice cloud models and their scattering properties are addressed through analyses of viewing angle dependence of retrieved ice cloud optical thickness, and an ice cloud model with mixed ice crystal habits is selected from 200 models. Conclusions are provided in §6.

Downloaded by [Texas A&M University Libraries and your student fees] at 08:16 22 December 2011

2. Ice cloud models and their sensitivity to the simulations of scattering properties and solar reflectances by cirrus clouds

2.1 *Ice cloud models*

Nearly all atmospheric ice crystals develop on the fundamental hexagonal matrix that results from the near tetrahedral bonding angles of the water molecule. Hexagonal ice crystals, in one form or another, are one of the most important ice crystal shapes within cirrus clouds. In this study, only HCs and HPs are assumed in developing an algorithm to determine optimal ice cloud models for satellite-based remote sensing of cirrus clouds. Other ice crystal habits such as bullet rosettes, droxtals, hollow columns and aggregates, often observed in clouds, could also be used for the ice cloud models to, perhaps, further improve their performance in retrieving ice cloud properties (Baum *et al.* 2003, 2005a,b). The habit fractions of ice crystals may have regional preferences and are strongly related to cloud temperature. This aspect may deserve future study but is beyond the aim of this work.

Hexagonal ice crystal geometries are normally specified by their aspect ratios, $\alpha = 2a/L$, where a and L are the semi-width and length of the ice particles, respectively. The aspect ratios of HCs used in this study are consistent with those of Mitchell and Arnott (1994) and can be formulated as follows:

$$\alpha = \begin{cases} 0.7 \text{ for } D < 100\,\mu\text{m} \\ 6.96L^{-0.5} \text{ for } D \geq 100\,\mu\text{m} \end{cases}, \tag{1}$$

where D represents the dimensions of the ice crystals and equals L for HCs. For HPs, the aspect ratios are determined based on *in situ* measurements of cirrus clouds (Auer and Veal 1970, Pruppacher and Klett 1980) and can be given by

$$\alpha = \begin{cases} 1 \text{ for } \mathrm{D} \leq 4\,\mu\text{m} \\ \dfrac{a}{0.2227a + 1.5547} \text{ for } 4\,\mu\text{m} < D < 10\,\mu\text{m} \\ 0.8038a^{0.526} \text{ for } D \geq 10\,\mu\text{m} \end{cases}, \tag{2}$$

where $D = 2a$.

Ice crystals with roughened surfaces or internal air bubbles are also considered here because they retain a simple hexagonal shape while significantly altering the optical

Downloaded by [Texas A&M University Libraries and your student fees] at 08:16 22 December 2011

properties. As in Yang *et al.* (2008b), the root mean square (RMS) tilt, σ, of the roughened facets on the ice crystal surfaces is used to specify the degree of roughness. Thus, the surface condition varies from smooth to severely rough as σ increases from 0 to 1. The geometries of inhomogeneous ice crystals have been described in detail by Xie *et al.* (2009) and will not be restated here in the interest of brevity. The internal air bubbles of the inhomogeneous ice crystals are simulated using spheroidal shapes that satisfy

$$\frac{x^2}{r_1^2} + \frac{y^2}{r_2^2} + \frac{z^2}{r_3^2} = 1, \tag{3}$$

where x, y and z represent the axes of x, y and z, respectively, and r_1, r_2 and r_3 are the air bubble semi-axes along the x, y and z directions, respectively. Here, r_1, r_2 and r_3 depend on the widths and lengths of the ice crystals as follows:

$$r_1 = C_{\text{bubble}} a, \tag{4}$$

$$r_2 = C_{\text{bubble}} a, \tag{5}$$

$$r_3 = C_{\text{bubble}} L, \tag{6}$$

where C_{bubble} is a constant.

For the ice cloud models, the ice crystal surface roughness condition and internal air bubbles are used for both the HC and HP cases. The geometric parameters σ and C_{bubble} are set to be 1.0 and 0.5, respectively, indicating a case with severely roughened ice crystals and a case with medium-sized air bubbles. Thus, the scattering properties of cirrus clouds are represented by ice cloud models consisting of six types of ice crystals including HC, surface-roughened column (RC), inhomogeneous column (IC), HP, surface-roughened plate (RP) and inhomogeneous plate (IP). Figure 1 compares the projected area and volume of these ice crystals as functions of ice crystal dimension. The degree of ice crystal surface roughness has not been considered in the computation of the projected areas and volumes of the ice crystals. As can be seen in figures 1(*a*) and (*b*), the projected areas of HP are much larger than HC when the dimensions are greater than 250 μm. However, the volume of HC is greater than HP in the region of 0–500 μm, as shown in figures 1(*c*) and (*d*). Note that the internal air bubbles within the ice crystals substantially reduce their volumes while having no effect on the projected areas.

To quantitatively characterize the cirrus cloud particle sizes, we use the effective particle size from

$$D_{\text{e}} = \frac{3}{2} \frac{\int_{D_{\min}}^{D_{\max}} V_{\text{total}}(D) n(D) \text{d}D}{\int_{D_{\min}}^{D_{\max}} A_{\text{total}}(D) n(D) \text{d}D}, \tag{7}$$

where $n(D)$ is the ice particle size distribution, $V_{\text{total}}(D)$ and $A_{\text{total}}(D)$ are the total volumes and projected areas of the ice crystals for size D, respectively, and $D_{\max}$ and $D_{\min}$ are the maximum and minimum values of D (Foot 1988). Following Baum *et al.* (2005a), the size distribution of ice cloud particles is represented by the gamma distribution given by

Downloaded by [Texas A&M University Libraries and your student fees] at 08:16 22 December 2011

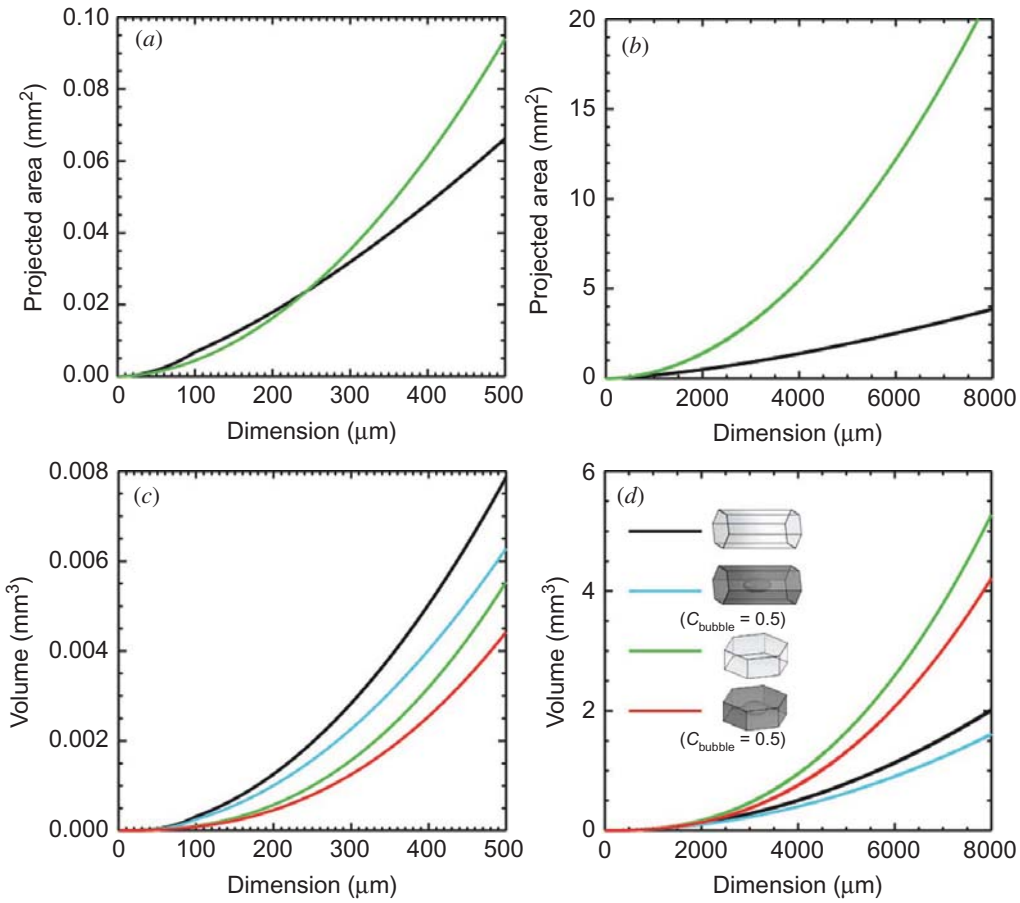

Figure 1. Ice crystal projected area versus dimension: (*a*, *b*) for HC (black) and HP (green) models and (*c*, *d*) variation of ice crystal volume versus dimension for HC (black lines), IC (blue), HP (green) and IP (red).

$$n(D) = N_0 D^{\mu} \exp\left(-\frac{b+\mu+0.67}{D_{\text{median}}} D\right), \tag{8}$$

where N_0 is the intercept, D_{median} is the median of the distribution of D, and μ and b are constants assumed to be 2.0 and 2.2, respectively. $V_{\text{total}}(D)$ and $A_{\text{total}}(D)$ in equation (7) are given as

$$\begin{aligned} V_{\text{total}}(D) = {} & C_{\text{HC}} V_{\text{HC}}(D) + C_{\text{RC}} V_{\text{RC}}(D) + C_{\text{IC}} V_{\text{IC}}(D) + \\ & C_{\text{HP}} V_{\text{HP}}(D) + C_{\text{RP}} V_{\text{RP}}(D) + C_{\text{IP}} V_{\text{IP}}(D), \end{aligned} \tag{9}$$

$$\begin{aligned} A_{\text{total}}(D) = {} & C_{\text{HC}} A_{\text{HC}}(D) + C_{\text{RC}} A_{\text{RC}}(D) + C_{\text{IC}} A_{\text{IC}}(D) + \\ & C_{\text{HP}} A_{\text{HP}}(D) + C_{\text{RP}} A_{\text{RP}}(D) + C_{\text{IP}} A_{\text{IP}}(D), \end{aligned} \tag{10}$$

where $V_{\text{HC}}(D)$, $V_{\text{RC}}(D)$, $V_{\text{IC}}(D)$, $V_{\text{HP}}(D)$, $V_{\text{RP}}(D)$ and $V_{\text{IP}}(D)$ and $A_{\text{HC}}(D)$, $A_{\text{RC}}(D)$, $A_{\text{IC}}(D)$, $A_{\text{HP}}(D)$, $A_{\text{RP}}(D)$ and $A_{\text{IP}}(D)$ are the volumes and projected areas, respectively, of the aforementioned ice crystal habits, denoted here by the subscripts; $C_{\text{HC}}(D)$, $C_{\text{RC}}(D)$, $C_{\text{IC}}(D)$, $C_{\text{HP}}(D)$, $C_{\text{RP}}(D)$ and $C_{\text{IP}}(D)$ are the corresponding habit fractions of the ice crystals. Thus, the goal of this study was to determine the appropriate

coefficients $C_{\mathrm{HC}}(D)$, $C_{\mathrm{RC}}(D)$, $C_{\mathrm{IC}}(D)$, $C_{\mathrm{HP}}(D)$, $C_{\mathrm{RP}}(D)$ or $C_{\mathrm{IP}}(D)$ by using satellite observations on a global scale.

2.2 *Sensitivity of ice cloud models to the simulations of their scattering properties*

For single ice crystals, the light scattering properties are simulated by an improved geometric optics method (IGOM) (Yang and Liou 1996b). After simulation, the scattering properties including scattering phase functions, $P_{11}(\Theta)$, extinction efficiencies, Q_{e}, and single-scattering albedos, ω, of an ensemble of ice crystals can be derived on the basis of ice crystal habit and size distributions as follows:

$$P_{11}(\Theta) = \frac{\int_{D_{\min}}^{D_{\max}} \left[\sum_i C_i P_{11,i}(\Theta, D) Q_{\mathrm{s},i}(D) A_i(D) \right] n(D) \mathrm{d}D}{\int_{D_{\min}}^{D_{\max}} \left[\sum_i C_i Q_{\mathrm{s},i}(D) A_i(D) \right] n(D) \mathrm{d}D}, \tag{11}$$

$$Q_{\mathrm{e}} = \frac{\int_{D_{\min}}^{D_{\max}} \left[\sum_i C_i Q_{\mathrm{e},i}(D) A_i(D) \right] n(D) \mathrm{d}D}{\int_{D_{\min}}^{D_{\max}} \left[\sum_i C_i A_i(D) \right] n(D) \mathrm{d}D}, \tag{12}$$

$$\omega = \frac{\int_{D_{\min}}^{D_{\max}} \left[\sum_i C_i Q_{\mathrm{s},i}(D) A_i(D) \right] n(D) \mathrm{d}D}{\int_{D_{\min}}^{D_{\max}} \left[\sum_i C_i Q_{\mathrm{e},i}(D) A_i(D) \right] n(D) \mathrm{d}D}, \tag{13}$$

where Θ is scattering angle, $P_{11,i}(\Theta)$ is the scattering phase function; $Q_{\mathrm{e},i}$ and $Q_{\mathrm{s},i}$ are the extinction and scattering efficiencies, respectively, for each ice crystal habit, and the subscripts i represent HC, RC, IC, HP, RP or IP.

Figure 2 compares the scattering phase functions of the ice cloud models for $D_{\mathrm{e}} = 50$ μm. To investigate the sensitivity of the phase function to ice cloud modes, each ice cloud model consists of only one ice crystal habit. Thus five of the habit fractions are 0 for each ice cloud model. From figure 2, HPs are seen to generally have larger forward scattering than HCs, although both ice cloud models have the same cloud particle size. Most HPs have larger projected areas than HCs for the same dimensions (see figure 1). Therefore, the diffraction of HPs is more significant than the scattering of light by the ice crystals. At a wavelength of $\lambda = 0.866$ μm (see figure 2(*a*)), the phase functions of HCs and HPs have strong forward and backward scattering and distinct halo peaks at the scattering angles near 22° and 46°. When surface roughness is introduced (i.e. RC and RP), the phase function halo features, caused by solar beams refracted by hexagonal ice crystals, completely vanish. Moreover, the forward and backward scattering of HCs and HPs are reduced due to light beam spreading in the refraction processes of the ice crystals (Yang *et al.* 2008b). As discussed by Xie *et al.* (2009), the inhomogeneity effect on the phase functions can also be seen for

Downloaded by [Texas A&M University Libraries and your student fees] at 08:16 22 December 2011

Downloaded by [Texas A&M University Libraries and your student fees] at 08:16 22 December 2011

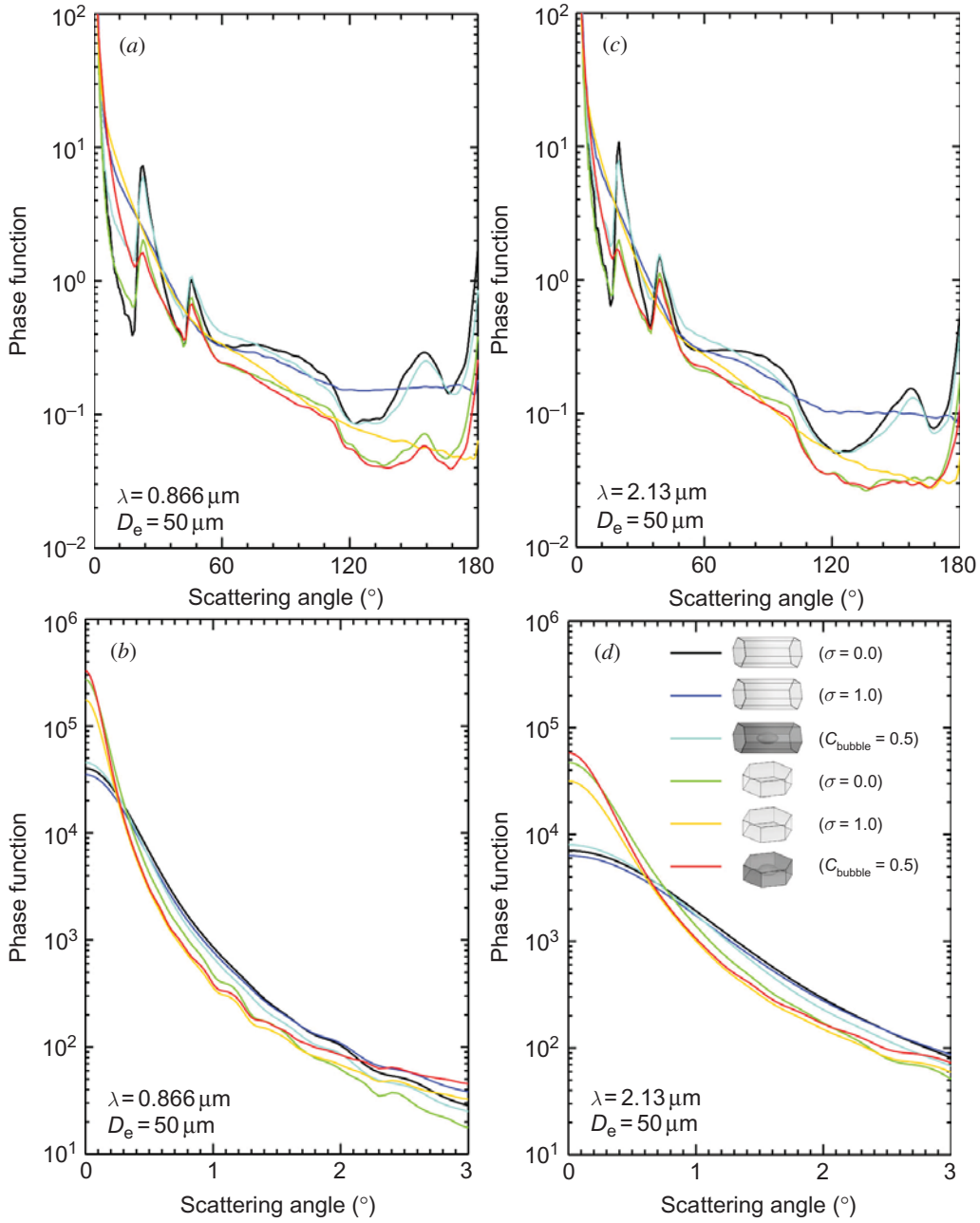

Figure 2. Scattering phase functions for HC (black), RC (blue), IC (cyan), HP (green), RP (yellow) and IP (red) models composed of randomly oriented ice crystals.

single ICs and IPs. However, the volumes of ICs and IPs are smaller than HCs and HPs because the volumes of air bubbles are subtracted. To achieve the same cloud effective particle sizes, inhomogeneous ice crystals in the ice cloud models have larger dimensions and larger aspect ratios than the homogeneous ones. Thus, the forward scattering of the IC and IP models is stronger than that for the HC and HP models, as shown in figure 2(*b*). Figures 2(*c*) and (*d*) compare the six phase functions of the ice cloud models at the wavelength of $\lambda = 2.13$ μm. At the near-infrared (NIR) wavelength, the smoothing of the scattering phase functions is shown for ice cloud models

consisting of RCs, RPs, ICs and IPs. At the NIR wavelength, the smoothing of the scattering phase functions for the RC, RP, IC and IP models relative to the homogeneous models is similar to that seen at 0.866 μm. As λ increases from 0.866 to 2.13 μm, the phase functions of the ice cloud models decrease in the forward scattering directions, because the ice crystal size diminishes relative to the wavelength.

2.3 *Sensitivity of solar reflectance to cirrus ice particle habit*

To retrieve ice cloud optical and microphysical properties, simulated cloud bidirectional reflectances are typically matched with satellite observations at solar wavelengths. Because the simulated cloud reflectances are sensitive to the particle habits used in the models, the retrieved properties will vary with the ice crystal scattering model used. This sensitivity needs to be quantified to understand its impact on the retrievals. The satellite-observed cloud bidirectional reflectance, R, is defined by

$$R(\mu_0, \mu, \varphi) = \frac{\pi I(\mu, \varphi)}{\mu_0 F}, \tag{14}$$

where F denotes the direct solar flux density at the top of the atmosphere (TOA), μ_0 and μ are the cosine values of the solar and satellite viewing zenith angles, θ_0 and θ, respectively, ϕ is the relative azimuth angle, and $I(\mu, \phi)$ is the radiance observed by the satellite instruments. The relative azimuth angle ϕ can be specified as follows:

$$\phi = \begin{cases} |\varphi - \varphi_0| \text{ for } 0^\circ \le |\varphi - \varphi_0| \le 180^\circ \\ 360^\circ - |\varphi - \varphi_0| \text{ for } |\varphi - \varphi_0| > 180^\circ \end{cases}, \tag{15}$$

where φ_0 and φ are the solar and satellite viewing azimuth angles, respectively.

Figure 3 shows the simulated cloud bidirectional reflectances using the six ice cloud models. The cloud reflectances were computed using discrete ordinates radiative transfer (DISORT) (Stamnes *et al.* 1988) assuming a homogenous ice cloud layer over a black surface, a cloud optical thickness of 1 and $\theta_0 = 30^\circ$. In each panel of figure 3, θ increases from 0° to 90° along the radial direction, and ϕ varies along the angular direction from 0° to 180°. At a wavelength of $\lambda = 0.866$ μm, figure 3(*a*) clearly shows that the cloud reflectance is sensitive to viewing geometries. At $\theta_0 = 30^\circ$, the maximum values of the cloud reflectances are associated with the forward directions where θ is between 80° and 90°. In the backscattering directions, the cloud reflectance maxima occur at $\theta = 30^\circ$ and are correlated to the phase function maxima at $\Theta = 180^\circ$. Clearly, the cloud reflectances in figure 3(*a*) are sensitive to the use of ice cloud models. For $\theta = 0^\circ$–45°, a range frequently used for satellite-based retrievals, the HP, RP and IP reflectances are much smaller than their columnar counterparts. This is probably due to the stronger forward scattering by plates (figure 2). The relative maxima at $\Theta = 180^\circ$ in the HC and HP phase functions (figure 2) yield the nearly pinpoint backscattering reflectance maxima seen in both figure 3(*a*) and (*b*). However, these maxima are significantly reduced for the inhomogeneous ice crystals and absent for the rough crystal reflectances as a result of their smoother phase functions. The sensitivity of cloud reflectances to the choice of ice cloud model is evident in the simulations at both wavelengths. Therefore, the ice crystal habit fractions in the ice cloud models will significantly affect the simulations of cloud reflectances and the retrieval of ice cloud properties.

Downloaded by [Texas A&M University Libraries and your student fees] at 08:16 22 December 2011

Downloaded by [Texas A&M University Libraries and your student fees] at 08:16 22 December 2011

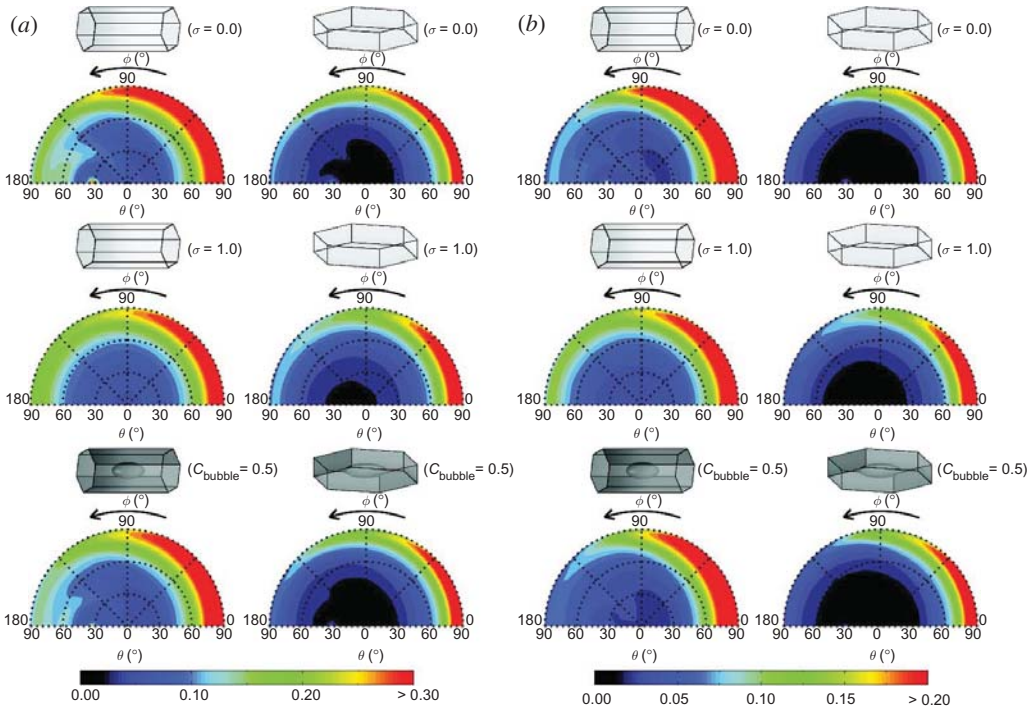

Figure 3. Cloud bidirectional reflectances computed for the HC, RC, IC, HP, RP and IP ice cloud models for $\theta_0 = 30°$, $D_e = 50$ μm and (*a*) $\lambda = 0.866$ μm and (*b*) $\lambda = 2.13$ μm.

3. Data and methodology

3.1 *Terra MODIS and MISR data*

Terra, launched on 18 December 1999, is a scientific research satellite component of the Earth Observing System (EOS). The MODIS instrument is designed to monitor the state of the Earth's environment including the radiation processes occurring in the atmosphere and at the Earth's surface. MODIS has 36 bands ranging in wavelength from 0.414 to 14.235 μm (Ardanuy *et al.* 1991). In this study, the MODIS bands centred at 0.86 and 2.13 μm are used to derive the ice cloud optical thickness and effective particle sizes over ocean because of the relatively small oceanic reflectance and atmospheric absorption at those wavelengths (Pinker and Laszlo 1992, Gatebe *et al.* 2005). In the retrieval process, the viewing and illumination geometries and reflectances at the TOA are provided by the MODIS Level 1B Calibrated Geolocation Data Set (MOD02) at a spatial resolution of 1 km × 1 km. The cloud thermodynamic phase is taken from the 1 km resolution cloud product (MOD06). The MOD02 and MOD06 data are stored in MODIS granules, each consisting of a 5-min data swath.

The Terra MISR instrument is designed to simultaneously provide measurements of daytime shortwave radiances from nine distinct cameras that view the nadir direction and the forward and aftward local vertical directions (Diner *et al.* 1989, 1998, 2002). MISR's cameras are designated as Df, Cf, Bf, Af, An, Aa, Ba, Ca and Da, where n denotes the nadir direction and f and a indicate whether the camera points forward or aftward along the Terra ground track. Except for the nadir camera, D, C, B and A represent the satellite viewing zenith angles of 70.5°, 60.0°, 45.6° and 26.1°, respectively. Each of the nine MISR cameras views the Earth in four spectral bands with central

Downloaded by [Texas A&M University Libraries and your student fees] at 08:16 22 December 2011

wavelengths at 0.446 (blue band), 0.558 (green band), 0.672 (red band) and 0.866 μm (NIR band) (Diner *et al.* 2002).

The Sun-synchronous Terra orbits have an exact 16-day repeating cycle. Because of this periodicity, MISR Level 1–2 data and data processing are divided into 233 discrete paths for the entire mission period. Each MISR path is further divided into 180 blocks with block 1 starting in the Arctic and block 180 ending in the Antarctic. Each block has a fixed sub-orbital area and corresponds to a fixed latitude, but the block number is a non-uniform function of latitude. The MISR Level 1B2 data (MI1B2T) and the retrieved reflecting level reference altitude (RLRA) values are used to develop the MISR Level 2 cloud product (MIL2TCAL), where the multi-angle reflectances from the nine cameras are registered at the height of the reflecting level (Diner *et al.* 1997, 1999). The 2.2 km resolution MIL2TCAL data are employed to derive ice cloud optical thicknesses using multi-angle cloud reflectance measurements.

Figure 4 shows an RGB (red–green–blue) image of MODIS radiances over the central Pacific Ocean acquired at 2050 Coordinated Universal Time (UTC) on 2 July 2009. The image was created using a MODIS Level 1B granule, which corresponds to 1354 × 2030 1 km pixels. The white boxes are the simultaneous MISR observation domains for blocks 78–95 in Path 60. In figure 4, the MISR region can be seen overlapped by the MODIS granule. By matching the MODIS data at 2.13 μm with the overlapping MISR data, it is possible to provide additional information, for example, particle size, to the MISR retrievals of ice cloud optical properties.

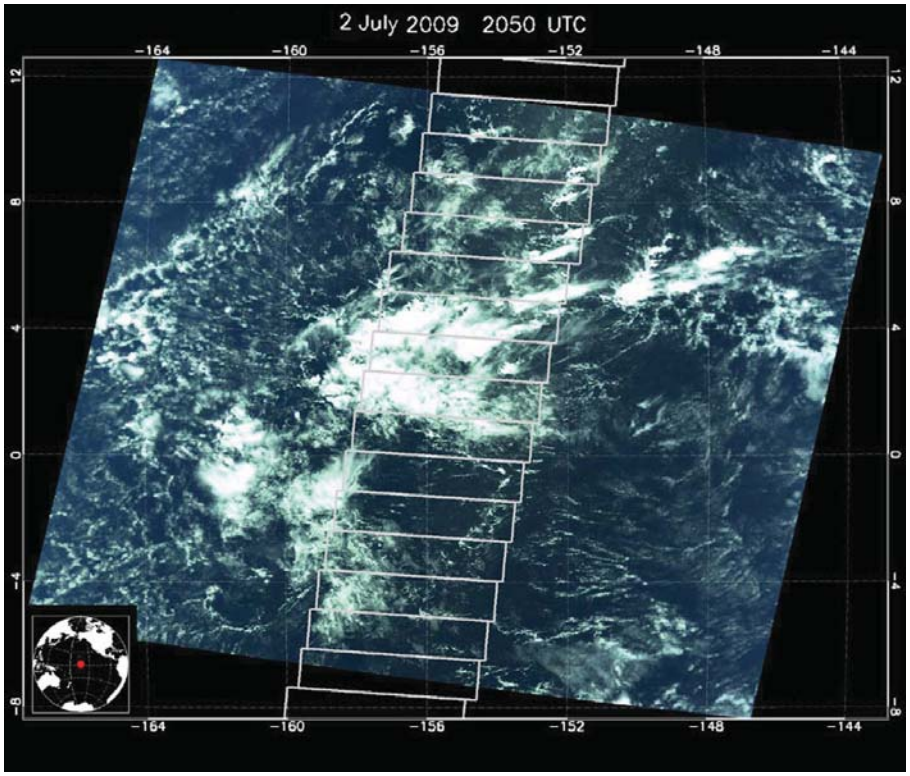

Figure 4. MODIS RGB (R for band 1; G for band 4; B for band 3) image over the central Pacific Ocean, 2050 UTC, 2 July 2009. The white boxes indicate blocks 78–95 of MISR Path 60.

Downloaded by [Texas A&M University Libraries and your student fees] at 08:16 22 December 2011

3.2 *Algorithm to retrieve ice cloud optical thickness using MODIS and MISR data*

The first step in determining the optimal ice cloud model is the retrieval of the ice cloud optical and microphysical properties. The cloud reflectances are simulated in MODIS bands 2 and 7 and the MISR NIR band for the cloud optical thickness $\tau = 0.05$, 0.1, 0.2, 0.5, 1.0, 2.0, 4.0, 6.0, 8.0, 10.0, 12.0, 14.0, 16.0, 18.0, 20.0, 25.0, 30.0, 35.0, 40.0 and 50.0. The cloud optical thicknesses at $\lambda = 0.866$ μm (hereafter referred to as $\tau_{0.866}$) are used as the reference optical thicknesses. The optical thicknesses at other wavelengths are related to $\tau_{0.866}$ by

$$\tau = \frac{Q_e}{Q_{e,0.866}} \tau_{0.866}, \tag{16}$$

where Q_e represents the extinction efficiency of a given ice cloud model and $Q_{e,0.866}$ is Q_e at $\lambda = 0.866$ μm. The solar and satellite viewing zenith angles are constructed using $\mu_0/\mu = 1.0$, 0.95, . . ., 0.0, and the relative azimuth angles ϕ are 0°, 2.5°, 5.0°, 10.0°, . . ., 175.0°, 177.5° and 180.0°.

Figure 5 shows a flow chart of the algorithm for retrieving ice cloud effective particle sizes using MODIS data. The simulated cloud reflectances, $R_{0.866}$ and $R_{2.13}$, are first interpolated in cloud optical thickness, particle size and solar and satellite viewing angles. For a cloud within a MODIS pixel, the thermodynamic phase is provided by the MOD06. The effective particle size of an ice cloud is initially assumed to be 100 μm. The value of $\tau_{0.866}$ is retrieved by matching the MOD02 band 2 reflectance to the reflectance simulated for each ice cloud model associated with $D_e = 100$ μm. A new effective particle size, D_{e2}, of the ice cloud is then computed using the MOD02 band 7 reflectance, and $\tau_{2.13}$ is determined with equation (16) using the retrieved $\tau_{0.866}$. The final retrieval of the cloud particle size is equal to its initial guess (D_{e1}) when $|D_{e1} - D_{e2}|$ is negligible. Otherwise, the retrieval process is repeated, using an adjusted D_{e1}, until the cloud effective particle size is retrieved or a specific stopping criterion is met.

Figure 6 shows the cloud thermodynamic phases and D_e retrieved using the HC model reflectances for the image in figure 4. The MODIS-retrieved cloud particle sizes within the MISR blocks can be used to retrieve the ice cloud optical thicknesses from MISR data. Figure 7 outlines the process for retrieving $\tau_{0.866}$ at different satellite viewing geometries. The retrieval is limited to MISR pixels over ocean overcast by ice clouds. The MODIS-retrieved cloud effective particle sizes, averaged over four contiguous MODIS pixels, are collocated with MISR pixels in 2.2 km × 2.2 km regions, when more than 70% of the MISR pixels are covered by the MODIS pixels. The 4-pixel D_e average is also compared with those for the surrounding 12 MODIS pixels to test the scene for uniformity. The cloud optical thickness retrieval is not performed when the D_e difference to the surrounding pixels exceeds 20 μm. The bias in cloud optical thickness caused by using an inappropriate D_e is discussed in §4. The collected D_e is used in cooperation with the MISR NIR band reflectance of MIL2TCAL and the simulated $R_{0.866}$ to derive $\tau_{0.866}$ for each MISR viewing geometry.

4. MODIS retrieval dependence of cloud optical thicknesses retrieved by MISR

The MODIS-retrieved cloud optical thicknesses are subject to uncertainties independent of the MODIS retrieval. As discussed in §3, cloud optical thicknesses and effective particle sizes are retrieved using cloud reflectances at visible and NIR wavelengths.

Downloaded by [Texas A&M University Libraries and your student fees] at 08:16 22 December 2011

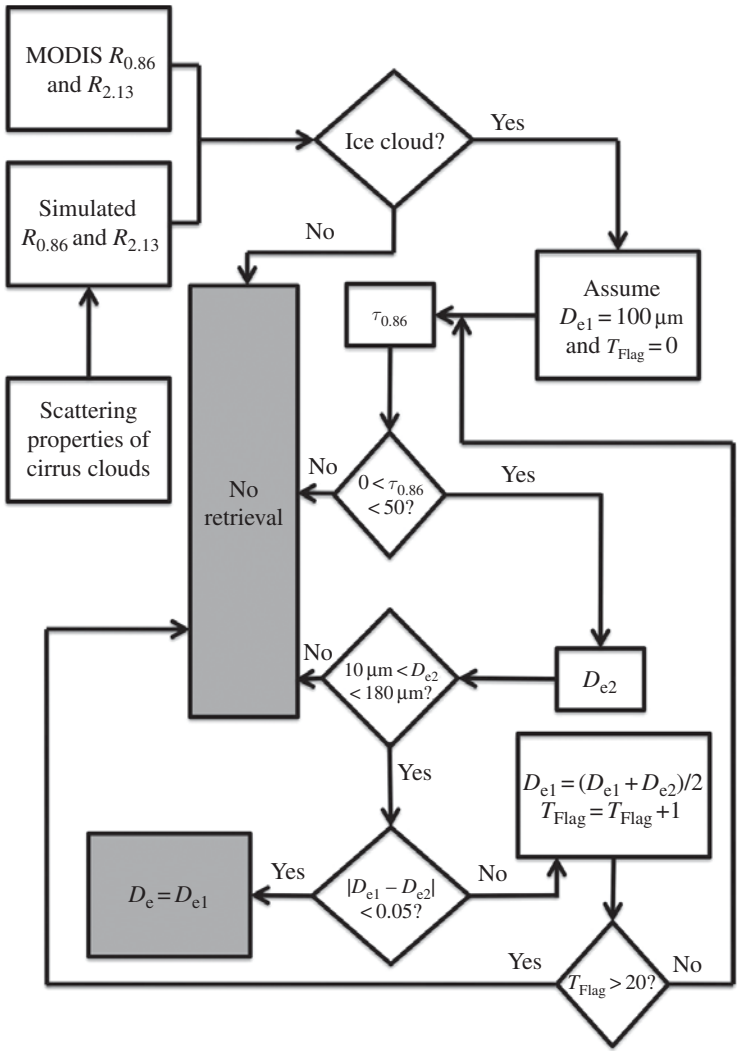

Figure 5. Flow chart of the algorithm for retrieving ice cloud effective particle sizes using MODIS data.

In the retrieval of τ, the derived cloud particle sizes are employed to match the model and observed reflectances. On the other hand, the retrieved cloud optical thicknesses can be used to compute the MODIS 2.13 μm reflectance to enhance the retrieval of D_e. This process can be applied iteratively to improve both the τ and D_e retrievals until the simulated cloud reflectances match the satellite observations. Therefore, biases in τ may be present when only the MISR NIR band reflectances are used in the retrievals.

To illustrate such errors, figure 8(*a*) plots the lookup table reflectances for the MODIS band 7 (black lines) and the MISR NIR band (red lines) for the HC model for two relative azimuth angles 85° (figure 8(*a*)) and 177.5° (figure 8(*b*)) where μ_0 and μ are both set to be 0.85. The red curves (MISR NIR reflectances) were computed using $D_e = 50$ μm. In figure 8(*a*), the retrieved cloud optical thicknesses are slightly overestimated when $D_e < 50$ μm. For clouds consisting of larger ice crystals, the retrieved cloud optical thicknesses with MISR NIR band reflectances are significantly underestimated. The bias caused by the absence of the MODIS band 7

Downloaded by [Texas A&M University Libraries and your student fees] at 08:16 22 December 2011

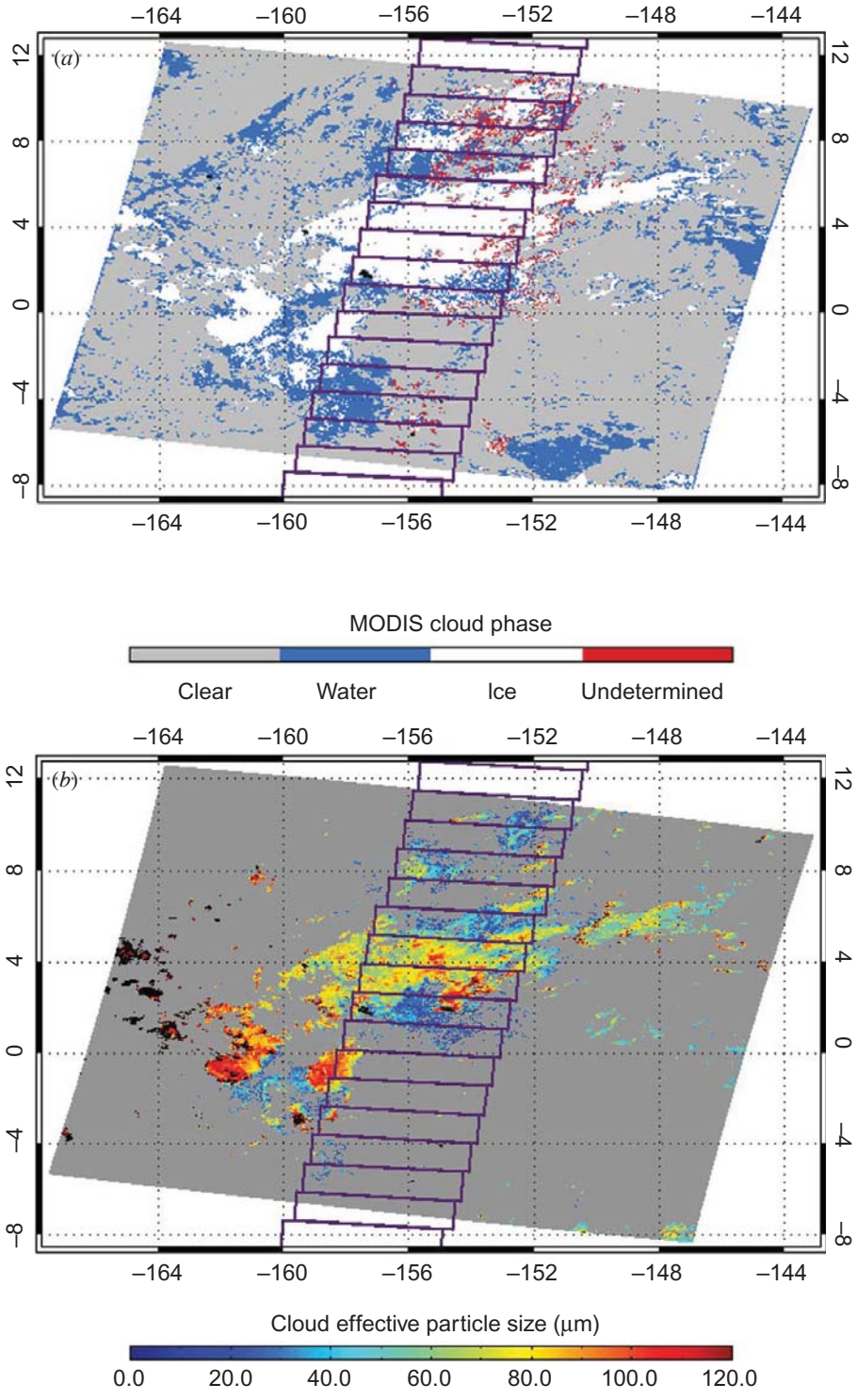

Figure 6. Cloud properties determined from radiances corresponding to the image in figure 4. (*a*) Thermodynamic phase and (*b*) ice cloud effective particle sizes derived using the HC ice cloud model.

reflectances varies with the ice cloud models and solar and satellite viewing geometries of the lookup tables. The lookup table reflectances plotted in figure 8(*b*) reveal that the errors in the cloud optical thicknesses using MISR data with $D_e = 50$ μm are more extreme when retrieved near the backscattering direction.

Downloaded by [Texas A&M University Libraries and your student fees] at 08:16 22 December 2011

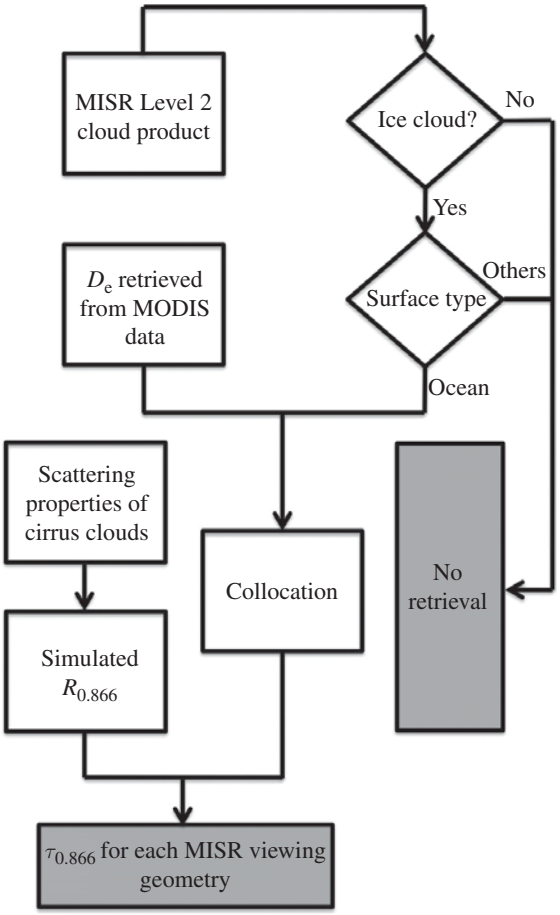

Figure 7. Flow chart of the algorithm for retrieving ice cloud optical thickness using matched MODIS and MISR data.

Figure 9 shows the relative errors in retrieved cloud optical thickness (RE_τ) using the six ice cloud models with $D_e = 50$ μm. These errors are defined as

$$RE_\tau = \frac{1}{N_\tau} \sum_{i=1}^{N_\tau} \frac{\tau_{MISR,i} - \tau_i}{\tau_i} 100\%, \tag{17}$$

where τ_i is the cloud optical thickness used to simulate the MODIS band 7 and MISR NIR band reflectances, $\tau_{MISR,i}$ is the optical thickness retrieved using the lookup table of MISR NIR band reflectances, with 'i' representing the number of the collocated pixels, and N_τ is the total number of τ_i for each D_e. Figures 9(*a*)–(*d*) show RE_τ averaged over the scattering angle, Θ, ranges 0°–45°, 45°–90°, 90°–135° and 135°–180°, respectively. In the region of forward scattering (see figure 9(*a*)), RE_τ is most sensitive to ice crystal habit and size. Fortunately, reflectances at $\Theta =$ 0°–45° are infrequently used in satellite-based remote sensing. The RE_τ at $\Theta = 45°$–90° is within ±10% for most of the models and particle sizes. For $\Theta = 90°$–135°, the RE_τ values for the column models are nearly 0% for $D_e < 60$ μm and reach −20% for the largest crystals. The RE_τ values for the plate models in figure 9(*c*) are positive for $D_e =$ 0–50 and 120–180 μm, indicating an overestimate of τ for such clouds. For $D_e =$ 50–120 μm, RE_τ is slightly smaller than 0. In the

Downloaded by [Texas A&M University Libraries and your student fees] at 08:16 22 December 2011

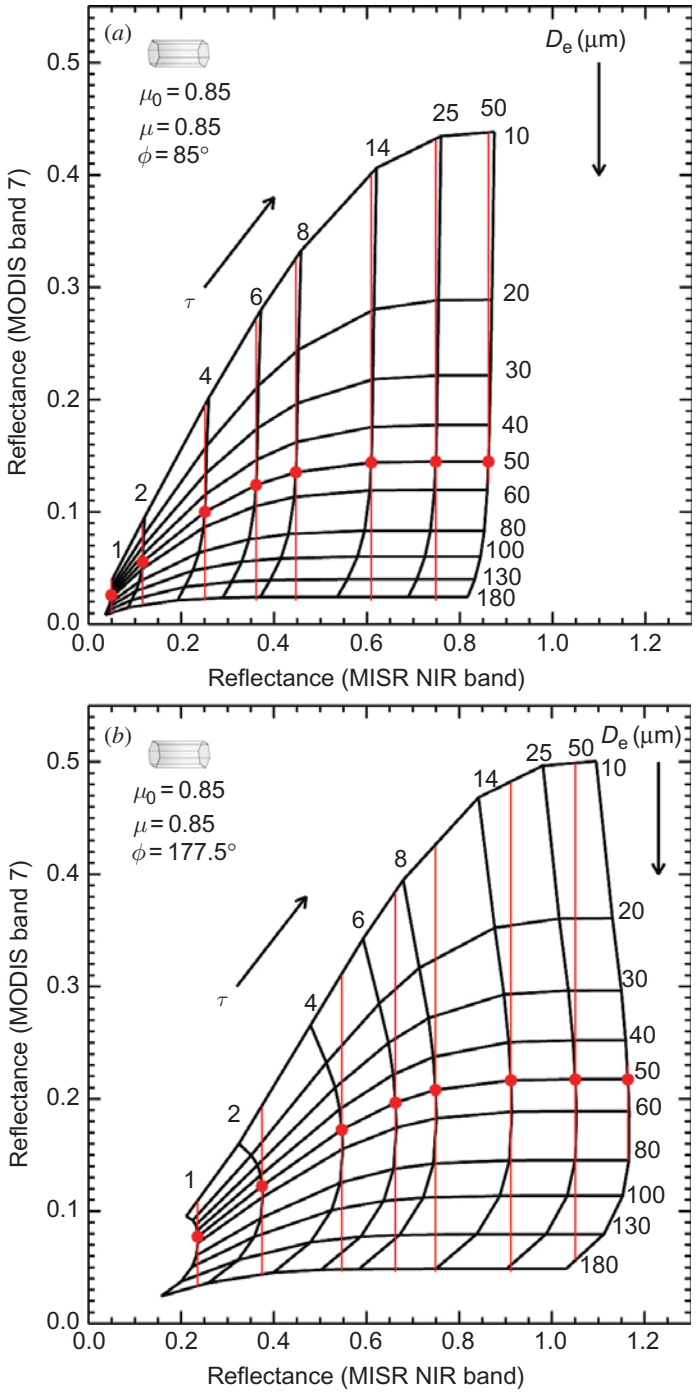

Figure 8. MODIS band 7 and MISR NIR band reflectances (black) for variable particle size and optical thickness and MISR NIR band reflectances (red) for $D_e = 50$ μm. All calculations performed for the HC model at $\mu_o = \mu = 0.85$ and $\phi =$ (*a*) 85°, (*b*) 177.5°.

region of backscattering (figure 9(*d*)), RE_τ for the column models is negligible. However, the optical thicknesses of plates are significantly underestimated when $D_e = 50$ μm is used in the retrieval.

From the results shown in figures 8 and 9, the average RE_τ values for the column models are within ±10% for the scattering angles related to satellite-based remote

Downloaded by [Texas A&M University Libraries and your student fees] at 08:16 22 December 2011

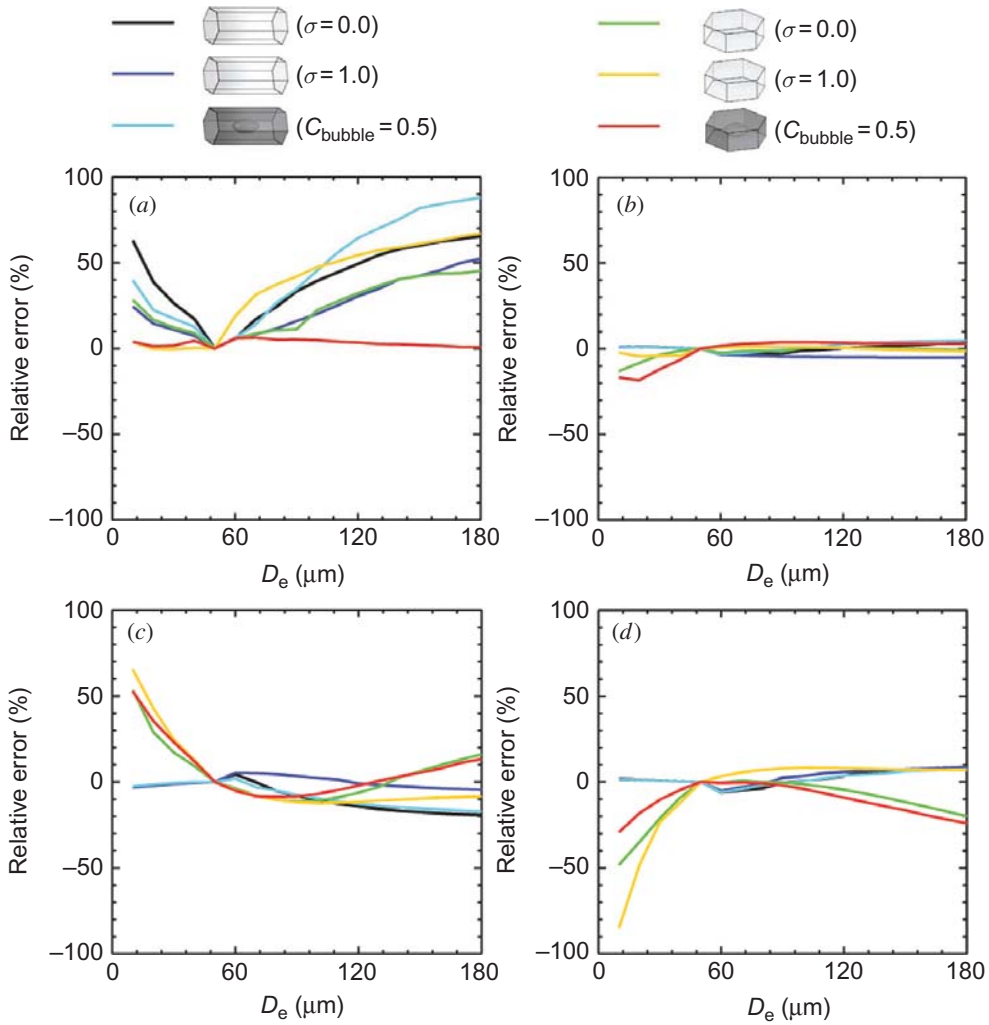

Figure 9. Relative errors in τ using HC, RC, IC, HP, RP and IP models with $D_e = 50$ μm and $\theta = (a)$ 0°–45°, (b) 45°–90°, (c) 90°–135° and (d) 135°–180°.

sensing. For plates, using an estimated cloud particle size may lead to substantial errors, especially for ice clouds with extremely small or large sizes. Thus, employing the MODIS retrieval of ice cloud effective particle sizes can efficiently remove the MISR retrieval biases that would otherwise result from the assumption of a constant particle size in the retrievals.

5. Results

Based on the algorithm described in §3, τ is retrieved for the nine MISR viewing geometries for the matched MODIS and MISR pixels. The difference between the cloud optical thicknesses from the nine viewing angles and their average can be used to evaluate the accuracy of the retrieval. With the presence of other uncertainties in the retrieval of ice cloud optical properties, the most appropriate ice cloud model will give the smallest optical thickness difference (OTD) values and RMS error ε of optical thickness and are formulated as follows:

$$\mathrm{OTD}_{i,j}=\frac{\tau_{i,j}-<\tau_i>_j}{<\tau_i>_j}, \tag{18}$$

$$\varepsilon=\sqrt{\frac{1}{9N_\mathrm{P}}\sum_{j=1}^{N_\mathrm{P}}\sum_{i=1}^{9}\mathrm{OTD}_{i,j}^2}, \tag{19}$$

where i is the number of the MISR viewing geometries, j is the number of collocated pixels, $\tau_{i,j}$ is the retrieved ice cloud optical thickness for each available MISR pixel, $<\tau_i>_j$ is the averaged value of $\tau_{i,j}$ over the nine MISR viewing geometries and N_P is the number of available MISR pixels.

5.1 *Errors in retrieved optical thickness for matched MODIS and MISR granule pixels*

Table 1 lists the values of ε for the matched MODIS and MISR data from the granules shown in figure 4 and those over the central Pacific Ocean on 19 February 2010 at 2140 UTC. For the retrievals using data from the granule in figure 4, the smallest error is clearly that for the RC model. The IP model yields the best performance in retrieving τ for the 19 February case. However, the retrieval errors for the HP, RP and RC models are not much greater than the IP minimum. Because of the natural variability of the cloud particle habits, the differences between the 2 July and 19 February results are not surprising.

Figure 10 shows the histograms of D_e and τ retrieved using the HC model for the matched MODIS and MISR data for the granules taken on 2 July 2009 and 19 February 2010. The distributions of D_e and τ for the data in figure 4 are centred at around 70 and 15 μm, respectively. For the retrievals using data from 19 February 2010, the particle sizes of the clouds are slightly smaller than 70 μm, and the maximum optical depth occurs around $\tau = 3$.

Because the RC model error is small for both days and has the least error for both days combined, it would be the most appropriate model overall for these two cases. The IP model has the lowest error for the 19 February case: its overall error is ∼19%, larger than that for the RC model. Because the IP model is the most appropriate for the 19 February case and the retrieved optical depths are, on average, considerably less than those retrieved for the 2 July case, it would appear that the IP or any of the

Table 1. RMS error, ε, of ice cloud optical thickness retrieved from matched MODIS and MISR data for one 5-min MODIS granule using six different models.

Ice cloud model	2050 UTC, 2 July 2009	2140 UTC, 2 July 2009
HC	0.2450	0.198
RC	0.1760	0.168
IC	0.2560	0.195
HP	0.2576	0.163
RP	0.2376	0.166
IP	0.2446	0.155

Downloaded by [Texas A&M University Libraries and your student fees] at 08:16 22 December 2011

Downloaded by [Texas A&M University Libraries and your student fees] at 08:16 22 December 2011

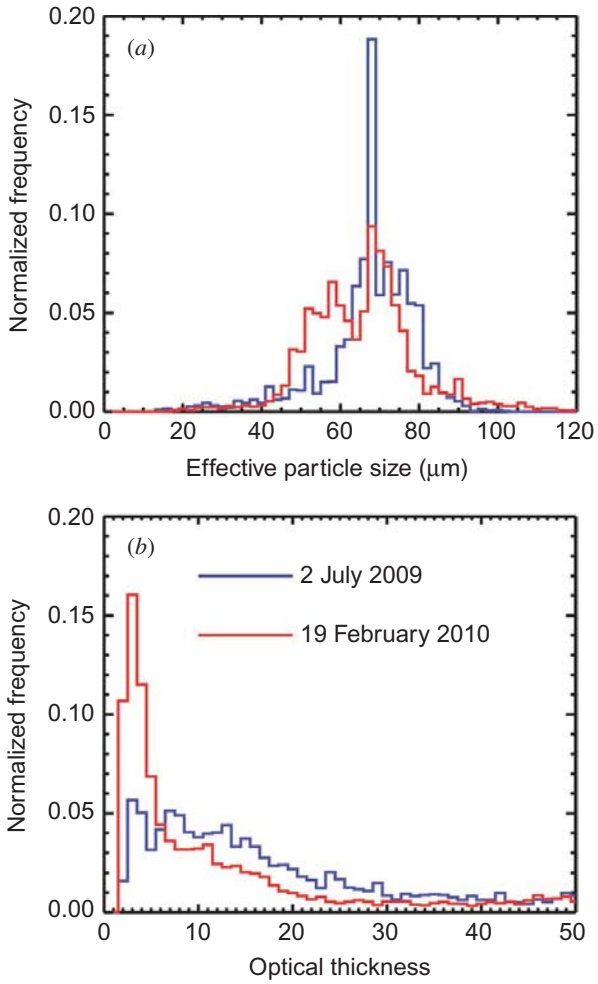

Figure 10. Histograms of the ice cloud (*a*) effective particle size and (*b*) optical thickness retrieved using the HC model for the granules taken on 2 July 2009 and 19 February 2010.

plate models would be best for optically thin clouds. However, the RC model error is only 8% greater than ε(IP) for that case. Thus, the use of plates to optimally retrieve τ for optically thin clouds is somewhat ambiguous. Further classification of the errors according to optical depth range would be required to determine whether the model errors vary with τ.

5.2 *Examination of ice cloud models using 1-day matched MODIS and MISR data*

To further examine the potential of finding an ice cloud model that produces the least biased retrievals of ice cloud properties, models containing various mixtures of the six ice crystal models were tested using MODIS and MISR data on a global scale. Following the results above using the two granules of matched MODIS and MISR data, RC data are assumed to be the major component for the habit mixtures. The habit fractions of the ice crystals in the ice cloud models are specified as follows:

$$C_{\mathrm{RC}} = 0.4 + 0.6\xi_1, \tag{20}$$

Downloaded by [Texas A&M University Libraries and your student fees] at 08:16 22 December 2011

$$C_{\mathrm{HC}} = \frac{(1 - C_{\mathrm{RC}})\xi_2}{\xi_2 + \xi_3 + \xi_4 + \xi_5 + \xi_6}, \tag{21}$$

$$C_{\mathrm{IC}} = \frac{(1 - C_{\mathrm{RC}})\xi_3}{\xi_2 + \xi_3 + \xi_4 + \xi_5 + \xi_6}, \tag{22}$$

$$C_{\mathrm{HP}} = \frac{(1 - C_{\mathrm{RC}})\xi_4}{\xi_2 + \xi_3 + \xi_4 + \xi_5 + \xi_6}, \tag{23}$$

$$C_{\mathrm{RP}} = \frac{(1 - C_{\mathrm{RC}})\xi_5}{\xi_2 + \xi_3 + \xi_4 + \xi_5 + \xi_6}, \tag{24}$$

$$C_{\mathrm{IP}} = \frac{(1 - C_{\mathrm{RC}})\xi_6}{\xi_2 + \xi_3 + \xi_4 + \xi_5 + \xi_6}, \tag{25}$$

where $\xi_1, \xi_2, \xi_3, \xi_4, \xi_5$ and ξ_6 are independent random numbers uniformly distributed in [0, 1].

Two hundred sets of habit fractions were initially examined using the two cases of 2 July and 19 February. Table 2 lists the habit mixture models having the minimum RMS errors in τ for C_{RC} varying within the fractional intervals (0.4, 0.5), (0.5, 0.6), (0.6, 0.7), (0.7, 0.8), (0.8, 0.9) and (0.9, 1.0). The RMS errors of cloud optical thickness generally decrease with increasing C_{RC}, which is associated with the overall low error ($\sim$0.172) of the RC model for the two cases combined. Including some fraction of other habits in the mixture only reduces the minimum two-case error by 0.6% (models M1 and M2) compared to the pure RC model.

Among the ice cloud models in this study, those consisting of a single ice crystal habit and M1, M3, M5, M7, M9 and M11 are further tested using all daytime matched MODIS and MISR data taken over ocean on 2 July 2009. A total of 129 MODIS granules and 15 MISR paths are involved. Figure 11 shows the histograms of D_{e} and τ retrieved using the HC model applied to the global 2 July data set. Compared to figure 10(*a*), the distribution of the cloud particle sizes in figure 11(*a*) is populated with ice particles covering a broad range with a peak at 60 μm. For the retrieved cloud optical thickness, the peak of the distribution occurs near 4, with $\sim$50% of the population having $\tau < 15$. The retrieved ice cloud properties in figure 11 are based on 244 611 2.2 km MISR pixels, which indicates that more than 100 and 2000 retrievals contribute to any interval displayed in figure 11(*a*) and (*b*), respectively. The large number of samples from all over the globe confirms that the results for this 1-day data set are much more representative of ice clouds over the globe than the two cases of 2 July and 19 February.

Figure 12 compares the ice cloud optical thicknesses derived using MISR measurements at nine different viewing angles. The retrievals of τ for figure 12 were obtained using the RC model. The optical thickness for each MISR viewing angle i, $<\tau>_i$, is specified by

Downloaded by [Texas A&M University Libraries and your student fees] at 08:16 22 December 2011

Table 2. Ice cloud models and RMS errors of cloud optical thickness for the MODIS and MISR granules on 2 July 2009 and 19 February 2010.

Ice cloud model	C_{HC}	C_{RC}	C_{IC}	C_{HP}	C_{RP}	C_{IP}	ε
			$0.9 < C_{RC} < 1.0$				
M1	0.0001	0.9974	0.0014	0.0009	0.0002	0.0000	0.171
M2	0.0023	0.9828	0.0034	0.0067	0.0003	0.0045	0.171
			$0.8 < C_{RC} < 0.9$				
M3	0.0423	0.8913	0.0004	0.0115	0.0063	0.0482	0.171
M4	0.0004	0.8848	0.0115	0.0063	0.0485	0.0485	0.172
			$0.7 < C_{RC} < 0.8$				
M5	0.0353	0.7963	0.0390	0.0598	0.0158	0.0538	0.172
M6	0.0270	0.7875	0.0584	0.0723	0.0045	0.0503	0.172
			$0.6 < C_{RC} < 0.7$				
M7	0.0589	0.6987	0.0361	0.0710	0.0374	0.0979	0.173
M8	0.0068	0.6817	0.0759	0.0807	0.0228	0.1321	0.173
			$0.5 < C_{RC} < 0.6$				
M9	0.0701	0.5217	0.0191	0.0779	0.1609	0.1503	0.174
M10	0.0190	0.5389	0.0775	0.1602	0.1495	0.0549	0.174
			$0.4 < C_{RC} < 0.5$				
M11	0.0091	0.4818	0.0066	0.0254	0.2528	0.2243	0.174
M12	0.0057	0.4026	0.0221	0.2196	0.1948	0.1552	0.174

$$\langle\tau\rangle_{\mathrm{i}} = \begin{cases} \frac{1}{N_{\mathrm{P1}}}\sum_{j=1}^{N_{\mathrm{P1}}}\tau_{i,j} & \text{for } \langle\tau\rangle \le 1 \\ \frac{1}{N_{\mathrm{P2}}}\sum_{j=1}^{N_{\mathrm{P2}}}\tau_{i,j} & \text{for } 1 < \langle\tau\rangle \le 2 \\ \frac{1}{N_{\mathrm{P3}}}\sum_{j=1}^{N_{\mathrm{P3}}}\tau_{i,j} & \text{for } 2 < \langle\tau\rangle \le 3 \\ \frac{1}{N_{\mathrm{P4}}}\sum_{j=1}^{N_{\mathrm{P4}}}\tau_{i,j} & \text{for } 3 < \langle\tau\rangle \le 4 \\ \frac{1}{N_{\mathrm{P5}}}\sum_{j=1}^{N_{\mathrm{P5}}}\tau_{i,j} & \text{for } 4 < \langle\tau\rangle \le 7 \\ \frac{1}{N_{\mathrm{P6}}}\sum_{j=1}^{N_{\mathrm{P6}}}\tau_{i,j} & \text{for } 7 < \langle\tau\rangle \le 15 \\ \frac{1}{N_{\mathrm{P7}}}\sum_{j=1}^{N_{\mathrm{P7}}}\tau_{i,j} & \text{for } 15 < \langle\tau\rangle \le 30 \\ \frac{1}{N_{\mathrm{P8}}}\sum_{j=1}^{N_{\mathrm{P8}}}\tau_{i,j} & \text{for } 30 < \langle\tau\rangle \end{cases}, \tag{26}$$

Downloaded by [Texas A&M University Libraries and your student fees] at 08:16 22 December 2011

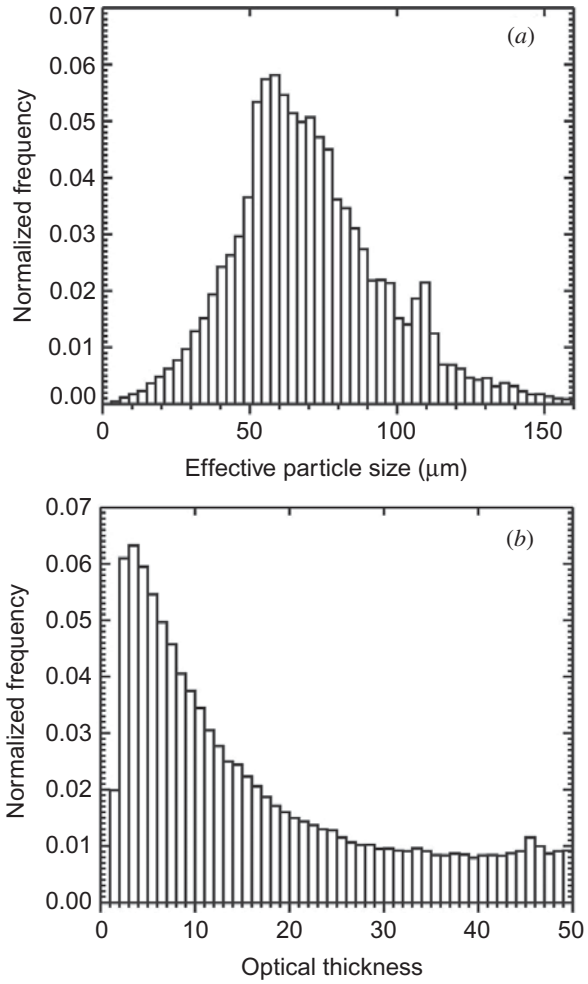

Figure 11. Same as figure 10, except for 1-day data taken over ocean, 2 July 2009.

where $<\tau>$ is the averaged value of $<\tau>_i$ over the nine MISR viewing angles and N_{P1}, N_{P2}, N_{P3}, N_{P4}, N_{P5}, N_{P6}, N_{P7} and N_{P8} are the numbers of MISR pixels for each interval of $<\tau>$. At $0° < \theta_0 < 45°$, the retrieved τ is slightly dependent on satellite viewing geometries, particularly when $<\tau> < 10$ (see figure 12(*a*)). The agreement between the retrievals developed at small solar zenith angles is related to the phase function being less sensitive to ice cloud models in the backscattering directions. For $45° < \theta_0 < 90°$ and the relative azimuth angle ϕ_{Df} of the MISR Df camera between 170° and 180°, retrievals developed over small viewing angles agree more with $<\tau>$, whereas the retrieved ice cloud optical thicknesses tend to be overestimated and underestimated fore and aft of the local vertical directions (see figure 12(*b*)). The effect can be explained by cloud-side illumination and shadowing by 3D clouds (Davies 1984, Loeb and Davies 1997, Loeb and Coakley 1998, Iwabuchi and Hayasaka 2002).

Figure 13 shows the normalized densities of ice cloud OTDs as functions of Θ retrieved using a water cloud model (figure 13(*a*)) and the HC model (figure 13(*b*)) for 263 657 and 244 611 MISR pixels, respectively. Mie theory (Wiscombe 1977) was used to compute the scattering properties of water cloud particles, whose refractive indices are $1.3244 + i3.58 \times 10^{-7}$ and $1.2901 + i3.94 \times 10^{-4}$ for $\lambda = 0.866$ μm and $\lambda = 2.13$ μm, respectively. Generally, the RMS values of the normalized OTDs in

Downloaded by [Texas A&M University Libraries and your student fees] at 08:16 22 December 2011

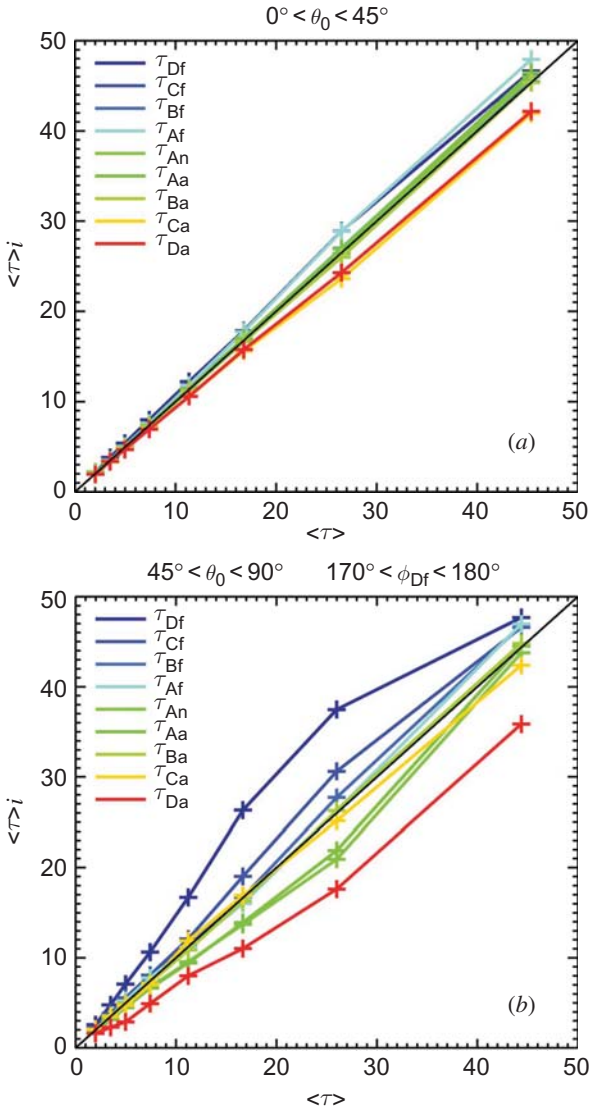

Figure 12. Average ice cloud optical thicknesses retrieved for each of the nine MISR cameras (denoted by the subscripts) using the RC model for 1-day matched MODIS and MISR data taken over ocean, 2 July 2009: (*a*) $0° < \theta_0 < 45°$ and (*b*) $45° < \theta_0 < 90°$ and $170° < \phi_{Df} < 180°$.

figure 13 are much larger than those derived for the two granules examined earlier (see tables 1 and 2) because the population of optically thick clouds is larger for the global data set. The ε resulting from retrievals based on the water cloud model is significantly larger than that from using the ice cloud model. In addition, compared to figure 13(*a*), the OTDs derived using the HC model are more symmetrical around a zero-bias line. These results confirm that the water cloud model is not appropriate for retrieving ice cloud optical properties, a conclusion reached from other types of analyses (e.g. Minnis *et al.* 1993, Doutriaux-Boucher *et al.* 2000).

Figures 14 and 15 show the normalized densities of ice cloud OTDs retrieved using the HC, RC and IC models as functions of Θ. The OTDs for the RC model are smaller and more symmetrical around the zero-bias line than those for the other two models. It is evident from the close-up plot in figure 15 that more MISR retrievals using the RC scattering properties are associated with OTDs in the range of −0.01 to 0.01.

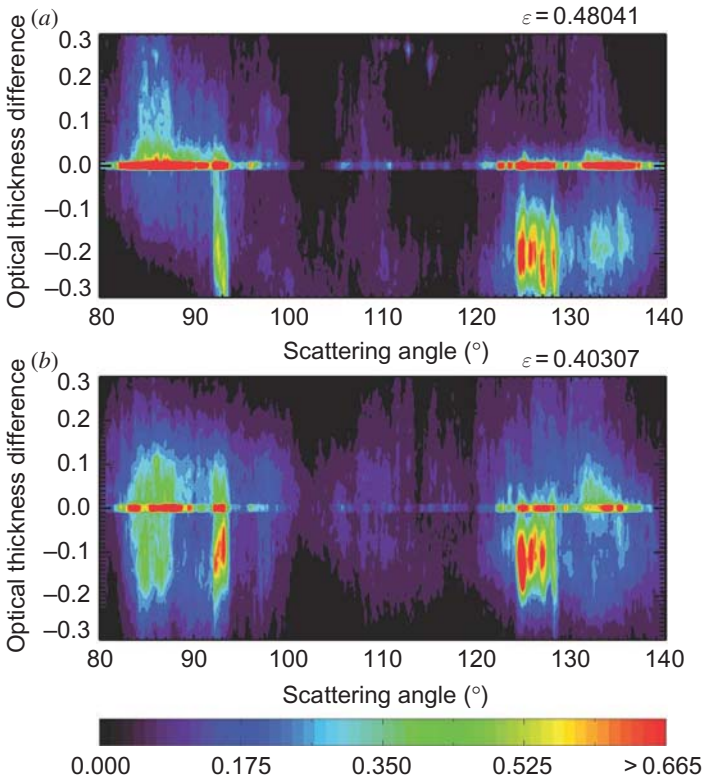

Figure 13. Normalized densities of ice cloud OTDs using (*a*) water cloud model and (*b*) HC model for 1-day matched MODIS and MISR data taken over ocean, 2 July 2009.

Figures 16 and 17 show the normalized densities of ice cloud OTDs using the HP, RP and IP models as functions of Θ. Compared to the results in figure 14, fewer valid retrievals were obtained using the plate models. None of the plate models yield the degree of OTD symmetry about the zero bias that was found for the RC model retrievals. Overall, among the six ice crystal habits used for the results in figures 14–17, the RC model yields the least angular dependence of the τ retrieval on viewing angle. This is consistent with the initial test of ice cloud models using the two MODIS granules.

Table 3 lists the average RMS errors of retrieved τ for all the ice cloud models tested using the 1-day MODIS–MISR data set. The smallest value of ε, 0.365, is found for the M3 model. Figure 18(*a*) shows that the normalized densities of M3 OTD produce a pattern similar to that found using the RC model (figure 14(*b*)). Figure 18(*b*) and (*c*) displays the OTD frequency differences between the M3 and HC results and the M3 and RC results as functions of Θ. The OTD distribution from M3 is quite different from that for the HC retrievals. Conversely, the M3 and RC distributions are very similar as indicated by the frequent occurrence of small differences in figure 18(*c*). From the comparison of OTDs between the M3 and RC results and their small differences in ϵ from table 3, it can be concluded that the M3 is minimally better at retrieving an angularly consistent τ. The asymmetry factors, g, of the ice cloud models are listed in table 4. For $D_e = 50$ μm, it can be found that g generally decreases when roughened surface and internal air bubbles are accounted for, which is consistent with the results reported by Yang *et al.* (2008b) and Xie *et al.* (2009). At $\lambda = 0.866$ and 2.13 μm, ε does

Downloaded by [Texas A&M University Libraries and your student fees] at 08:16 22 December 2011

Downloaded by [Texas A&M University Libraries and your student fees] at 08:16 22 December 2011

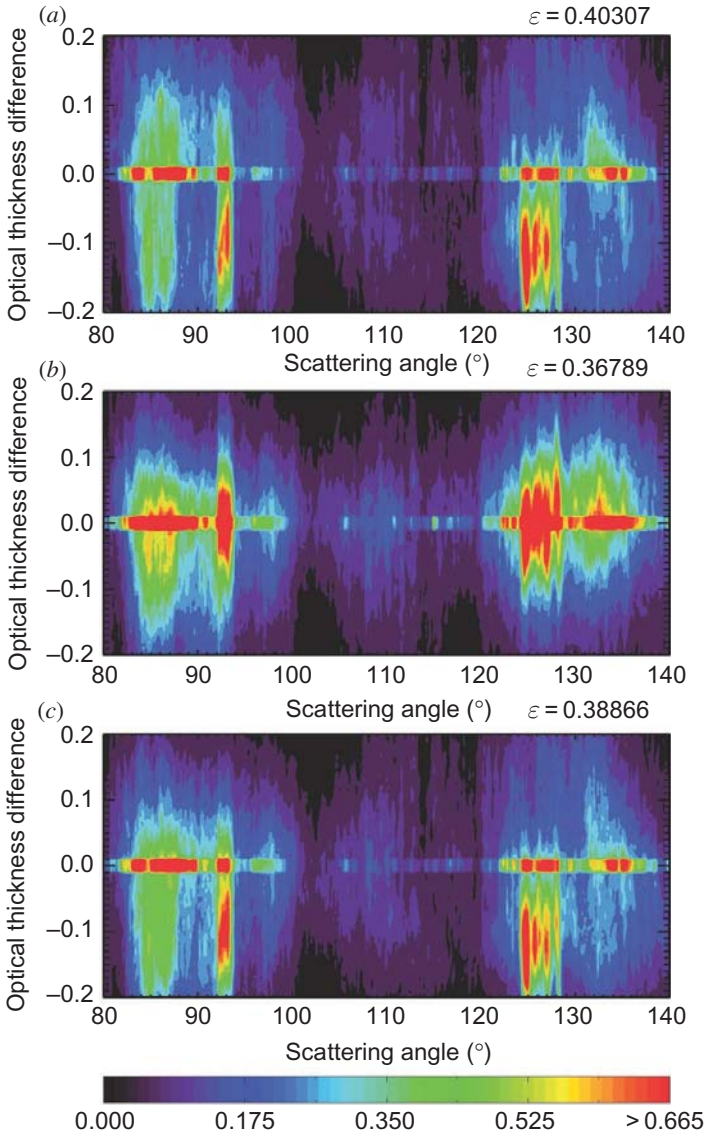

Figure 14. Same as figure 13, except using (*a*) HC, (*b*) RC and (c) IC models.

not have a linear relationship with g, as is evident from tables 3 and 4. However, ice cloud models with relatively small g normally have better performance in the retrieval of ice cloud properties.

Figure 19 replots the normalized densities of the M3 OTDs for two different ranges of $<\tau>$, 0–5 (figures 19(*a*)) and 5–20 (figure 19(*b*)). From figure 19, it is evident that the M3 model performed well in retrieving ice cloud properties for both optically thin and thick clouds. Based on the comparison between the data in figures 19(*a*) and (*b*), the OTDs of optically thin cirrus clouds are concentrated closer to 0. The greater errors for optically thick cirrus cloud retrievals may, in part, be due to a greater contribution of 3D effects (Iwabuchi and Hayasaka 2002).

From these results, it can be concluded that among the tested ice crystal distributions, the M3 model is the best model for retrieving cloud optical thickness from solar reflectance measurements. However, its accuracy is only slightly better than that found

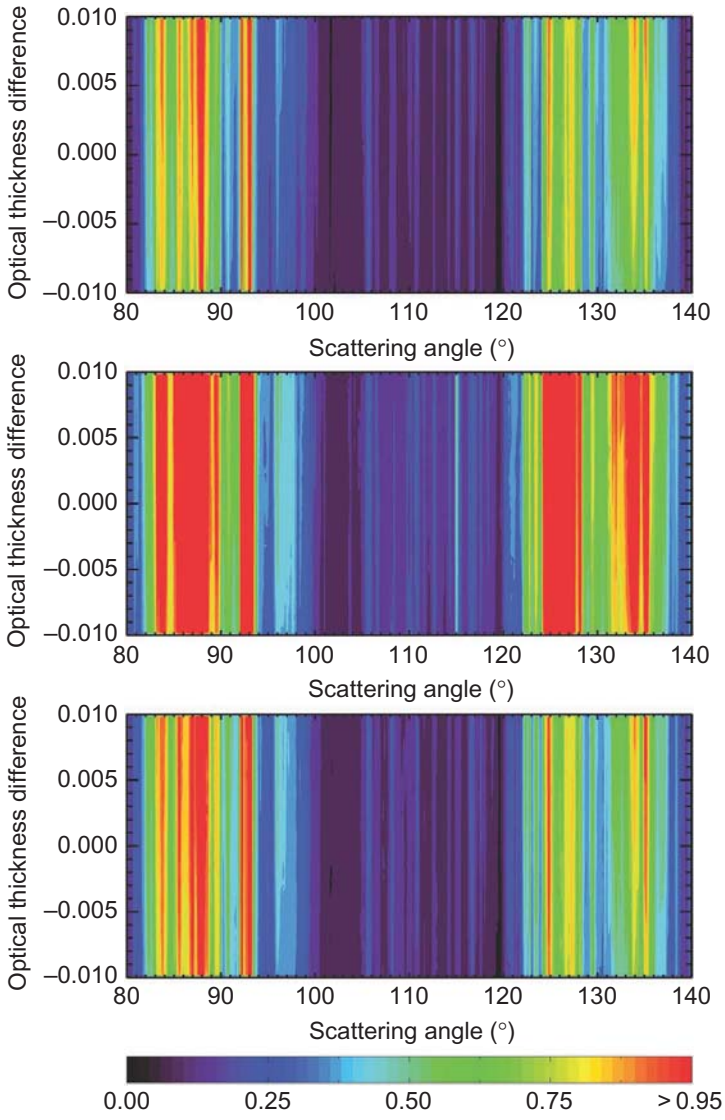

Figure 15. Same as figure 14, except only for normalized OTDs between −0.01 and 0.01.

for the simpler roughened hexagonal ice column model, RC, and three other habit-mixture models. All five represent significant improvements over the use of smooth HCs and HPs, roughened plates and IPs. The goal of this study was to determine the optimal model for simple shapes and combinations of those simple shapes. As noted earlier, many other habits and combinations of habits are possible, and they may yield smaller dependencies of the retrieved τ on the viewing and illumination geometry. However, much additional study is required to examine the sensitivity of the retrieved optical thickness to more complex shapes and combinations.

6. Summary

In this study, we examined a broad range of ice cloud models that consist of smooth, roughened, homogeneous and inhomogeneous hexagonal ice crystals with various aspect ratios. The sensitivity of cirrus bulk scattering properties and solar reflectances

Downloaded by [Texas A&M University Libraries and your student fees] at 08:16 22 December 2011

Downloaded by [Texas A&M University Libraries and your student fees] at 08:16 22 December 2011

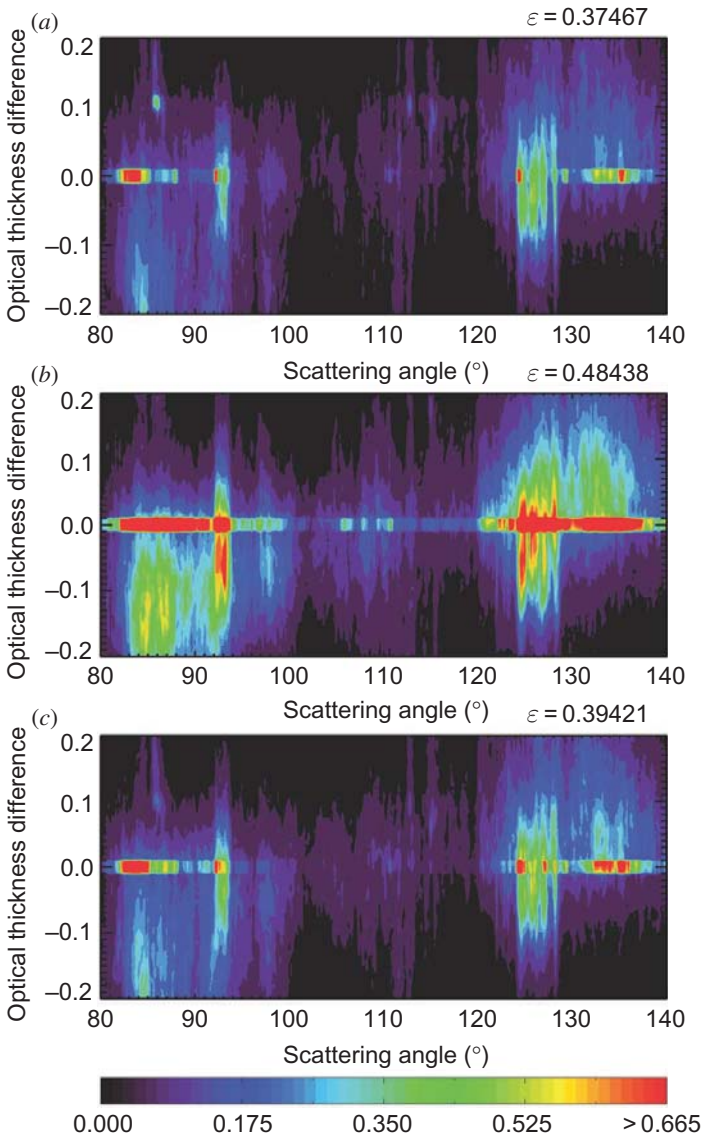

Figure 16. Same as figure 14, except for using (*a*) HP, (*b*) RP and (*c*) IP models.

to these ice cloud models was investigated using the IGOM and DISORT models. At shortwave wavelengths, the smoothed scattering phase function was shown for ice cloud models with surface-roughened or inhomogeneous ice crystals. It was also demonstrated that cloud bidirectional reflectance is sensitive to the particular ice cloud habit with the smoothest reflectance fields resulting from the use of severely roughened ice columns.

The MODIS cloud reflectances from bands 1 and 7, averaged over $1^\circ \times 1^\circ$ latitude–longitude regions, are consistent with those in MISR red and NIR bands. An algorithm was developed to retrieve ice cloud optical thickness using matched MODIS and MISR data. The MODIS data are used to derive ice cloud particle size. The retrieved ice cloud particle sizes are then collocated to the MISR pixel for cloud optical thickness retrievals at the nine MISR views. Errors in cloud property retrievals are examined when MODIS retrievals are not provided. For the solar

Downloaded by [Texas A&M University Libraries and your student fees] at 08:16 22 December 2011

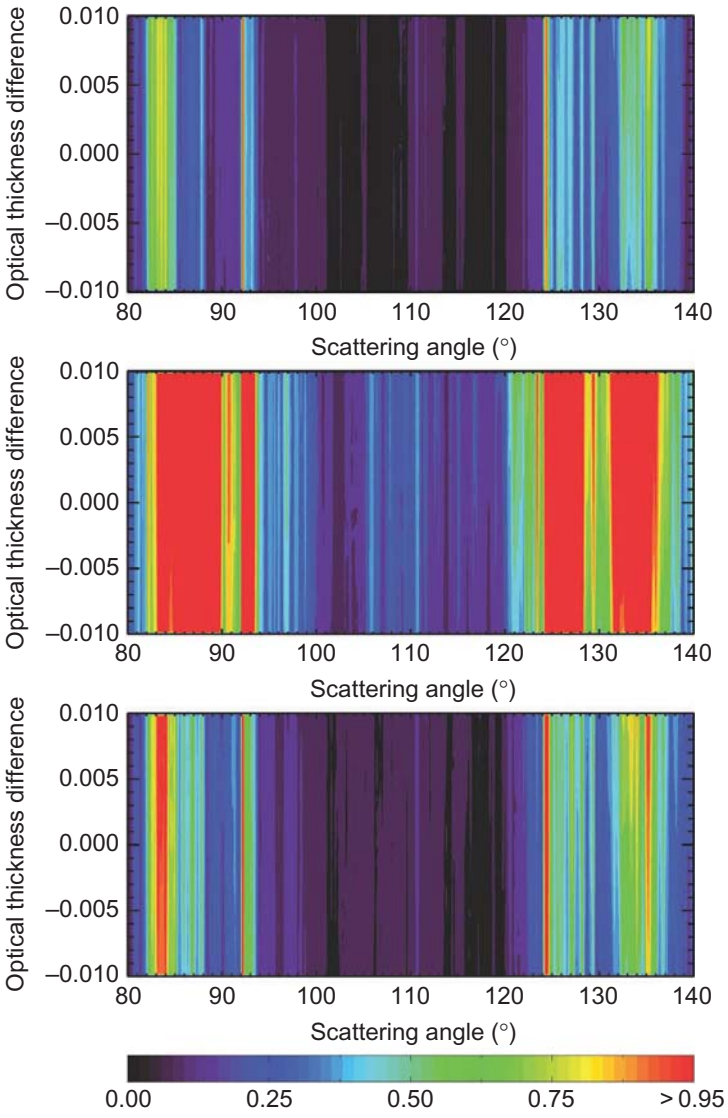

Figure 17. Same as figure 16, except only for normalized OTDs between −0.01 and 0.01.

Table 3. Ice cloud models and RMS errors of cloud optical thickness for the MODIS and MISR granules at a 1-day interval on 2 July 2009.

Ice cloud model	ε	Ice cloud model	ε
HC	0.403	M1	0.367
RC	0.368	M3	0.365
IC	0.389	M5	0.366
HP	0.375	M7	0.369
RP	0.484	M9	0.388
IP	0.394	M11	0.407

Downloaded by [Texas A&M University Libraries and your student fees] at 08:16 22 December 2011

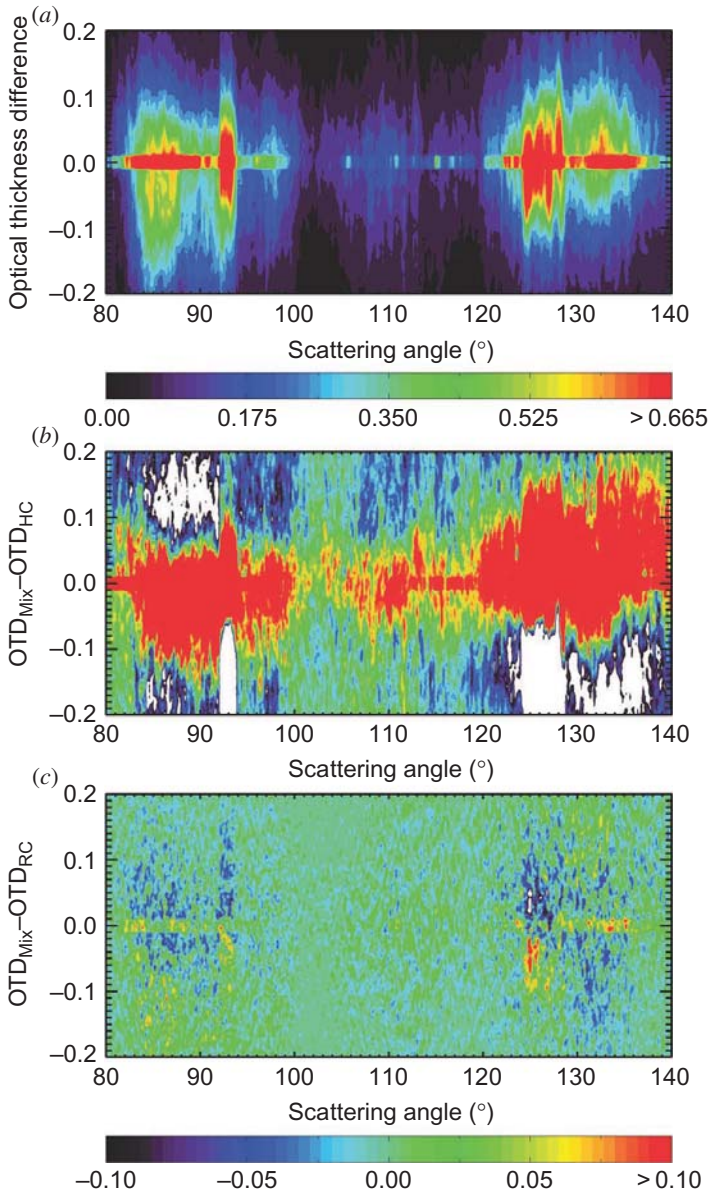

Figure 18. (*a*) Normalized density of ice cloud OTDs using the M3 model, (*b*) $OTD_{Mix} - OTD_{HC}$ and (*c*) $OTD_{Mix} - OTD_{RC}$ as functions of scattering angle for 1-day matched MODIS and MISR data taken over ocean, 2 July 2009.

and satellite viewing angles applied most closely to the operational conditions in cloud property retrievals, the relative errors in cloud optical thickness are within ±10% when the ice cloud model consists of only columns. For the plate ice cloud model, substantial errors may arise from the absence of MODIS retrievals of cloud particle size. Therefore, particle size-dependent biases can be efficiently removed by using the MODIS-retrieved particle size in the MISR retrieval of ice cloud optical thickness.

The ice cloud optical thicknesses are retrieved for the nine MISR viewing geometries in the overlap regions of MODIS and MISR granules. The differences between cloud optical thickness retrieved at the nine views and their mean are used to characterize

Table 4. Ice cloud models and their asymmetry factors for $D_e = 50$ μm.

Ice cloud model	g ($\lambda = 0.866$ μm)	g ($\lambda = 2.13$ μm)
HC	0.7938	0.8452
RC	0.7820	0.8309
IC	0.7862	0.8389
HP	0.9172	0.9352
RP	0.8529	0.8906
IP	0.9104	0.9286
M1	0.7822	0.8310
M3	0.7868	0.8351
M5	0.7916	0.8392
M7	0.7971	0.8439
M9	0.8091	0.8537
M11	0.8159	0.8589

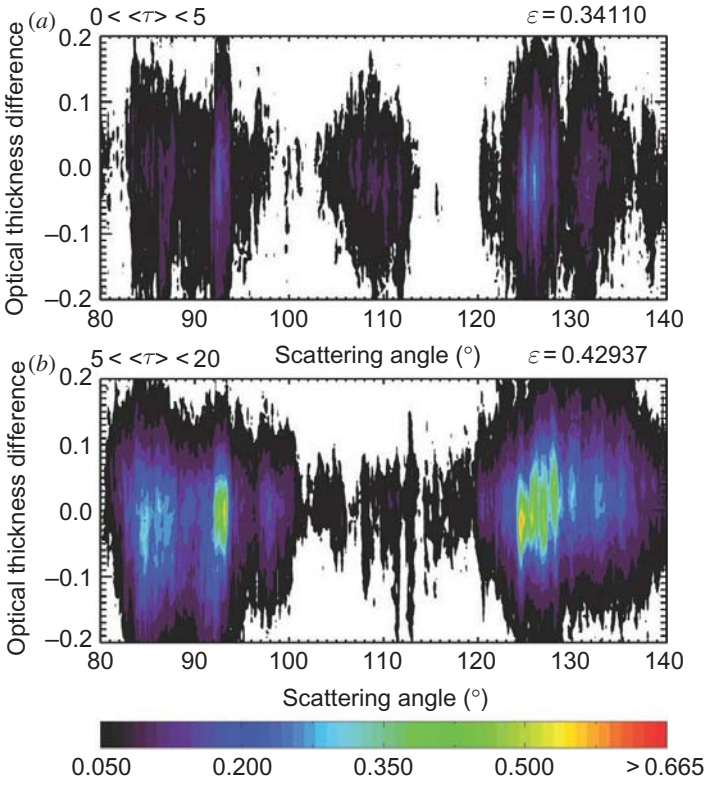

Figure 19. Normalized density of ice cloud OTDs using the M3 model: (*a*) $0 < <\tau> < 5$ and (*b*) $5 < <\tau> < 20$.

the retrieval accuracy. Ice cloud models containing single and mixed ice crystal habits are initially examined using MODIS and MISR data at two 5-min intervals. The ice cloud model with RCs has the best overall performance in fitting the reflectances with the cloud property retrievals. The ice cloud models are further tested using the daytime MODIS and MISR data taken over ocean for the entire day of 2 July 2009. The retrieved ice cloud optical thicknesses tend to be overestimated and underestimated fore and aft of the local vertical directions. Employing mixtures of inhomogeneous

Downloaded by [Texas A&M University Libraries and your student fees] at 08:16 22 December 2011

and homogeneous ice crystals with surface roughness is found to further reduce the uncertainty in the ice cloud retrievals, but only by a small amount. A new ice cloud model containing a mixture of ice crystal habits or a distribution of severely roughened hexagonal ice columns is recommended for future satellite-based retrievals of ice cloud properties for both optically thin and thick clouds.

Acknowledgements

This study was partly supported by NASA grants NNX09AP63G and NNX10AL55G. George W. Kattawar's research was supported by the Office of Naval Research under contracts N00014-06-1-0069 and N00014-11-1-0154. Patrick Minnis was supported by the NASA SMD Radiation Sciences Program through the Clouds and the Earth's Radiant Energy System Project. The work by Dong L. Wu was performed at the Jet Propulsion Laboratory, California Institute of Technology, under contract with NASA.

Downloaded by [Texas A&M University Libraries and your student fees] at 08:16 22 December 2011

References

Ardanuy, P.E., Han, D. and Salomonson, V.V., 1991, The Moderate Resolution Imaging Spectrometer (MODIS) science and data system requirements. *IEEE Transactions on Geoscience and Remote Sensing*, **29**, pp. 75–88.

Arnott, W.P., Dong, Y.Y., Hallett, J. and Poellot, M.R., 1994, Role of small ice crystals in radiative properties of cirrus: a case study, FIRE II, November 22, 1991. *Journal of Geophysical Research*, **99**, pp. 1371–1381.

Auer, A.H. and Veal, D.L., 1970, Dimension of ice crystals in natural clouds. *Journal of the Atmospheric Sciences*, **27**, pp. 919–926.

Bailey, M. and Hallett, J., 2004, Growth rates and habits of ice crystals between −20° and −70°C. *Journal of the Atmospheric Sciences*, **61**, pp. 514–544.

Baker, B.A. and Lawson, R.P., 2006, In situ observations of the microphysical properties of wave, cirrus, and anvil clouds. Part I: wave clouds. *Journal of the Atmospheric Sciences*, **63**, pp. 3160–3185.

Baran, A.J., Francis, P.N., Labonnote, L.C. and Doutriaux-Boucher, M., 2001a, A scattering phase function for ice cloud: tests of applicability using aircraft and satellite multi-angle multi-wavelength radiance measurements of cirrus. *Quarterly Journal of the Royal Meteorological Society*, **127**, pp. 2395–2416.

Baran, A.J. and Labonnote, L.C., 2006, On the reflection and polarisation properties of ice cloud. *Journal of Quantitative Spectroscopy & Radiative Transfer*, **100**, pp. 41–54.

Baran, A.J., Shcherbakov, V.N., Baker, B.A., Gayet, J.F. and Lawson, R.P., 2005, On the scattering phase-function of non-symmetric ice-crystals. *Quarterly Journal of the Royal Meteorological Society*, **131**, pp. 2609–2616.

Baran, A.J., Yang, P. and Havemann, S., 2001b, Calculation of the single-scattering properties of randomly oriented hexagonal ice columns: a comparison of the T-matrix and the finite-difference time-domain methods. *Applied Optics*, **40**, pp. 4376–4386.

Baum, B.A., Frey, R.A., Mace, G.G., Harkey, M.K. and Yang, P., 2003, Nighttime multilayered cloud detection using MODIS and ARM data. *Journal of Applied Meteorology*, **42**, pp. 905–919.

Baum, B.A., Heymsfield, A.J., Yang, P. and Bedka, S.T., 2005a, Bulk scattering properties for the remote sensing of ice clouds. Part I: microphysical data and models. *Journal of Applied Meteorology*, **44**, pp. 1885–1895.

Baum, B.A., Kratz, D.P., Yang, P., Ou, S.C., Hu, Y.X., Soulen, P.F. and Tsay, S.C., 2000, Remote sensing of cloud properties using MODIS airborne simulator imagery during SUCCESS. Part I: data and models. *Journal of Geophysical Research*, **105**, pp. 11767–11780.

Baum, B.A., Yang, P., Heymsfield, A.J., Platnick, S., King, M.D., Hu, Y.X. and Bedka, S.T., 2005b, Bulk scattering properties for the remote sensing of ice clouds. Part II: narrowband models. *Journal of Applied Meteorology*, **44**, pp. 1896–1911.

Baum, B.A., Yang, P., Nasiri, S., Heidinger, A.K., Heymsfield, A. and Li, J., 2007, Bulk scattering properties for the remote sensing of ice clouds. Part III: high-resolution spectral models from 100 to 3250 cm^{-1}. *Journal of Applied Meteorology*, **46**, pp. 423–434.

Baumgardner, D., Chepfer, H., Raga, G.B. and Kok, G.L., 2005, The shapes of very small cirrus particles derived from in situ measurements. *Geophysical Research Letters*, **32**, L01806, doi:10.1029/2004GL021300.

Cai, Q. and Liou, K.N., 1982, Polarized-light scattering by hexagonal ice crystals: theory. *Applied Optics*, **21**, pp. 3569–3580.

Chepfer, H., Goloub, P., Riedi, J., De Haan, J.F., Hovenier, J.W. and Flamant, P.H., 2001, Ice crystal shapes in cirrus clouds derived from POLDER/ADEOS-1. *Journal of Geophysical Research*, **106**, pp. 7955–7966.

Chepfer, H., Minnis, P., Young, D., Nguyen, L. and Arduini, R.F., 2002, Estimation of cirrus cloud effective ice crystal shapes using visible reflectances from dual-satellite measurements. *Journal of Geophysical Research*, **107**, p. 4730.

Chepfer, H., Noel, V., Minnis, P., Baumgardner, D., Nguyen, L., Raga, G., McGill, M.J. and Yang, P., 2005, Particle habit in tropical ice clouds during CRYSTAL-FACE: comparison of two remote sensing techniques with in situ observations. *Journal of Geophysical Research*, **110**, D16204, doi:10.1029/2004JD005455.

Coleman, R.F. and Liou, K.N., 1981, Light scattering by hexagonal ice crystals. *Journal of the Atmospheric Sciences*, **38**, pp. 1260–1271.

Davies, R., 1984, Reflected solar radiances from broken cloud scenes and the interpretation of scanner measurements. *Journal of Geophysical Research*, **89**, pp. 1259–1266.

Diner, D.J., Beckert, J.C., Bothwell, G.W. and Rodriguez, J.I., 2002, Performance of the MISR instrument during its first 20 months in Earth orbit. *IEEE Transactions on Geoscience and Remote Sensing*, **40**, pp. 1449–1466.

Diner, D.J., Beckert, J.C., Reilly, T.H., Bruegge, C.J., Conel, J.E., Kahn, R.A., Martonchik, J.V., Ackerman, T.P., Davies, R., Gerstl, S.A.W., Gordon, H.R., Muller, J.P., Myneni, R.B., Sellers, P.J., Pinty, B. and Verstraete, M.M., 1998, Multi-angle Imaging SpectroRadiometer (MISR) instrument description and experiment overview. *IEEE Transactions on Geoscience and Remote Sensing*, **36**, pp. 1072–1087.

Diner, D.J., Bruegge, C.J., Martonchik, J.V., Ackerman, T.P., Davies, R., Gerstl, S.A.W., Gordon, H.R., Sellers, P.J., Clark, J., Daniels, J.A., Danielson, E.D., Duval, V.G., Klaasen, K.P., Lilienthal, G.W., Nakamoto, D.I., Pagano, R.J. and Reilly, T.H., 1989, MISR: a multiangle imaging spectroradiometer for geophysical and climatological research from Eos. *IEEE Transactions on Geoscience and Remote Sensing*, **27**, pp. 200–214.

Diner, D.J., Davies, R., Girolamo, L.D., Horvath, A., Moroney, C., Muller, J.P., Paradise, S.R., Wenkert, D. and Zong, J., 1997, *MISR Level 2 Aerosol Retrieval Algorithm Theoretical Basis*, JPL document D-11400, Rev. C (Pasadena, CA: Jet Propulsion Laboratory).

Diner, D.J., Davies, R., Varnai, T., Moroney, C., Borel, C., Gerstl, S. and Nealson, D., 1999, Level 2 top-of-atmosphere albedo algorithm theoretical basis. Available online at: http://hdl.handle.net/2014/18866 (accessed 11 February 1999).

Doutriaux-Boucher, M., Buriez, J.C., Brogniez, G., Labonnote, L.C. and Baran, A.J., 2000, Sensitivity of retrieved POLDER directional cloud optical thickness to various ice particle models. *Geophysical Research Letters*, **27**, pp. 109–112.

Foot, J.S., 1988, Some observations of the optical properties of clouds. II: Cirrus. *Quarterly Journal of the Royal Meteorological Society*, **114**, pp. 145–164.

Downloaded by [Texas A&M University Libraries and your student fees] at 08:16 22 December 2011

Downloaded by [Texas A&M University Libraries and your student fees] at 08:16 22 December 2011

Gatebe, C.K., King, M.D., Lyapustin, A.I., Arnold, G.T. and Redemann, J., 2005, Airborne spectral measurements of ocean directional reflectance. *Journal of the Atmospheric Sciences*, **62**, pp. 1072–1092.

Heymsfield, A.J., Bansemer, A., Field, P.R., Durden, S.L., Stith, J.L., Dye, J.E., Hall, W. and Grainger, C.A., 2002, Observations and parameterizations of particle size distributions in deep tropical cirrus and stratiform precipitating clouds: results from in situ observations in TRMM field campaigns. *Journal of the Atmospheric Sciences*, **59**, pp. 3457–3491.

Heymsfield, A.J., Miller, K.M. and Spinhirne, J.D., 1990, The 27–28 October 1986 FIRE IFO cirrus case study: cloud microstructure. *Monthly Weather Review*, **118**, pp. 2313–2328.

Heymsfield, A.J. and Miloshevich, L.M., 2003, Parameterizations for the cross-sectional area and extinction of cirrus and stratiform ice cloud particles. *Journal of the Atmospheric Sciences*, **60**, pp. 936–956.

Iwabuchi, H. and Hayasaka, T., 2002, Effects of cloud horizontal inhomogeneity on the optical thickness retrieved from moderate-resolution satellite data. *Journal of the Atmospheric Sciences*, **59**, pp. 2227–2242.

Jensen, E., Starr, D.O. and Toon, O.B., 2004, Mission investigates tropical cirrus clouds. *Eos, Transactions of the American Geophysical Union*, **85**, pp. 45–50.

Kajikawa, M. and Heymsfield, A.J., 1989, Aggregation of ice crystals in cirrus. *Journal of the Atmospheric Sciences*, **46**, pp. 3108–3121.

Kato, S. and Marshak, A., 2009, Solar zenith and viewing geometry-dependent errors in satellite retrieved cloud optical thickness: marine stratocumulus case. *Journal of Geophysical Research*, **114**, D01202, doi:10.1029/2008JD010579.

King, M.D., Platnick, S., Yang, P., Arnold, G.T., Gray, M.A., Riedi, J.C., Ackerman, S.A. and Liou, K.N., 2004, Remote sensing of liquid water and ice cloud optical thickness and effective radius in the Arctic: application of airborne multispectral MAS data. *Journal of Atmospheric and Oceanic Technology*, **21**, pp. 857–875.

King, M.D., Tsay, S.C., Platnick, S.E., Wang, M. and Liou, K.N., 1996, Cloud retrieval algorithms for MODIS: optical thickness, effective particle radius, and thermodynamic phase. In *MODIS Algorithm Theoretical Basis Document No. ATBD-MOD-05*. Available online at: http://modis.gsfc.nasa.gov/data/atbd/atbd_mod05.pdf

Kobayashi, T., 1961, The growth of snow crystals at low supersaturation. *Philadelphia Magazine*, **6**, pp. 1363–1370.

Korolev, A.V., Isaac, G.A. and Hallett, J., 1999, Ice particle habits in Arctic clouds. *Geophysical Research Letters*, **26**, pp. 1299–1302.

Labonnote, L.C., Brogniez, G., Buriez, J.C., Doutriaux-Boucher, M., Gayet, J.F. and Macke, A., 2001, Polarized light scattering by inhomogeneous hexagonal monocrystals: validation with ADEOS–POLDER measurements. *Journal of Geophysical Research*, **106**, pp. 12139–12153.

Lawless, R., Xie, Y. and Yang, P., 2006, Polarization and effective Mueller matrix for multiple scattering of light by nonspherical ice crystals. *Optics Express*, **14**, pp. 6381–6393.

Lawson, R.P., Baker, B., Pilson, B. and Mo, Q.X., 2006, In situ observations of the microphysical properties of wave, cirrus, and anvil clouds. Part II: cirrus clouds. *Journal of the Atmospheric Sciences*, **63**, pp. 3186–3203.

Li, J., Huang, H.L., Liu, C.Y., Yang, P., Schmit, T.J., Wei, H.L., Weisz, E., Guan, L. and Menzel, W.P., 2005, Retrieval of cloud microphysical properties from MODIS and AIRS. *Journal of Applied Meteorology and Climatology*, **44**, pp. 1526–1543.

Loeb, N.G. and Coakley, J.A., 1998, Inference of marine stratus cloud optical depths from satellite measurements: does 1D theory apply? *Journal of Climate*, **11**, pp. 215–233.

Loeb, N.G. and Davies, R., 1997, Angular dependence of observed reflectances: a comparison with plane parallel theory. *Journal of Geophysical Research*, **102**, pp. 6865–6881.

Downloaded by [Texas A&M University Libraries and your student fees] at 08:16 22 December 2011

Macke, A., 1993, Scattering of light by polyhedral ice crystals. *Applied Optics*, **32**, pp. 2780–2788.

Macke, A. and Mishchenko, M.I., 1996, Applicability of regular particle shapes in light scattering calculations for atmospheric ice particles. *Applied Optics*, **35**, pp. 4291–4296.

Masuda, K., Ishimoto, H. and Takashima, T., 2002, Retrieval of cirrus optical thickness and ice-shape information using total and polarized reflectance from satellite measurements. *Journal of Quantitative Spectroscopy and Radiative Transfer*, **75**, pp. 39–51.

McFarlane, S.A., Marchand, R.T. and Ackerman, T.P., 2005, Retrieval of cloud phase and crystal habit from Multiangle Imaging Spectroradiometer (MISR) and Moderate Resolution Imaging Spectroradiometer (MODIS) data. *Journal of Geophysical Research*, **110**, D14201, doi:10.1029/2004JD004831.

McFarquhar, G.M., Yang, P., Macke, A. and Baran, A.J., 2002, A new parameterization of single scattering solar radiative properties for tropical anvils using observed ice crystal size and shape distributions. *Journal of the Atmospheric Sciences*, **59**, pp. 2458–2478.

Minnis, P., Garber, D.P., Young, D.F. and Arduini, R.F., 1998, Parameterizations of reflectance and effective emittance for satellite remote sensing of cloud properties. *Journal of the Atmospheric Sciences*, **55**, pp. 3313–3339.

Minnis, P., Heck, P.W. and Young, D.F., 1993, Inference of cirrus cloud properties using satellite-observed visible and infrared radiances. Part II: verification of theoretical cirrus radiative properties. *Journal of the Atmospheric Sciences*, **50**, pp. 1305–1322.

Minnis, P., Sun-Mack, S., Young, D., Heck, P.W., Garber, D.P., Chen, Y., Spangenberg, D.A., Arduini, R.F., Trepte, Q.Z., Smith, W.L., Ayers, J.K., Gibson, S.C., Miller, W.F., Hong, G., Chakrapani, V., Takano, Y., Liou, K.N., Xie, Y. and Yang, P., 2011, CERES edition-2 cloud property retrievals using TRMM VIRS and TERRA and AQUA MODIS data, part I: algorithms. *IEEE Transactions on Geoscience and Remote Sensing*, **49**, pp. 4374–4400.

Minnis, P., Young, D., Sun-Mack, S., Heck, P.W., Doelling, D.R. and Trepte, Q.Z., 2004, CERES cloud property retrievals from imagers on TRMM, Terra, and Aqua. In *Proceedings of SPIE 10th International Symposium on Remote Sensing: Conference on Remote Sensing of Clouds and the Atmosphere VII*, 9 September 2003, Klaus P. Schäfer, Adolfo Comerón, Michel R. Carleer and Richard H. Picard (Eds.), Barcelona, Spain (Bellingham, WA: SPIE), pp. 37–48.

Mitchell, D.L. and Arnott, W.P., 1994, A model predicting the evolution of ice particle-size spectra and radiative properties of cirrus clouds. Part II: dependence of absorption and extinction on ice crystal morphology. *Journal of the Atmospheric Sciences*, **51**, pp. 817–832.

Nasiri, S.L., Baum, B.A., Heymsfield, A.J., Yang, P., Poellot, M.R., Kratz, D.P. and Hu, Y.X., 2002, The development of midlatitude cirrus models for MODIS using FIRE-I, FIRE-II, and ARM in situ data. *Journal of Applied Meteorology*, **41**, pp. 197–217.

Oreopoulos, L. and Davies, R., 1998, Plane parallel albedo biases from satellite observations. Part I: dependence on resolution and other factors. *Journal of Climate*, **11**, pp. 919–932.

Pinker, R.T. and Laszlo, I., 1992, Modeling surface solar irradiance for satellite applications on a global scale. *Journal of Applied Meteorology*, **31**, pp. 194–211.

Pruppacher, H.R. and Klett, J.D., 1980, *Microphysics of Clouds and Precipitation* (Boston, MA: Reidel).

Sassen, K., Knight, N.C., Takano, Y. and Heymsfield, A.J., 1994, Effects of ice-crystal structure on halo formation: cirrus cloud experimental and ray-tracing modeling studies. *Applied Optics*, **33**, pp. 4590–4601.

Silva Dias, M.A.F., Rutledge, S., Kabat, P., Dias, P.L.S., Nobre, C., Fisch, G., Dolman, A.J., Zipser, E., Garstang, M., Manzi, A.O., Fuentes, J.D., Rocha, H.R., Marengo, J., Plana-Fattori, A., Sa, L.D.A., Alvala, R.C.S., Andreae, M.O., Artaxo, P., Gielow, R. and Gatti, L., 2002, Cloud and rain processes in a biosphere–atmosphere interaction context in the Amazon region. *Journal of Geophysical Research*, **107**, 8072, doi:10.1029/2001JD000335.

Downloaded by [Texas A&M University Libraries and your student fees] at 08:16 22 December 2011

Stamnes, K., Tsay, S.C., Wiscombe, W. and Jayaweera, K., 1988, Numerically stable algorithm for discrete-ordinate-method radiative transfer in multiple scattering and emitting layered media. *Applied Optics*, **27**, pp. 2502–2509.

Starr, D.O., 1987, A cirrus-cloud experiment: intensive field observations planned for FIRE. *Bulletin of the American Meteorological Society*, **68**, pp. 119–124.

Sun, W.B., Loeb, N.G. and Yang, P., 2006, On the retrieval of ice cloud particle shapes from POLDER measurements. *Journal of Quantitative Spectroscopy and Radiative Transfer*, **101**, pp. 435–447.

Takano, Y. and Liou, K.N., 1995, Radiative transfer in cirrus clouds. Part III: light-scattering by irregular ice crystals. *Journal of the Atmospheric Sciences*, **52**, pp. 818–837.

Tape, W., 1994, *Atmospheric Halos* (Washington, D.C.: American Geophysical Union).

Wendisch, M., Yang, P. and Pilewskie, P., 2007, Effects of ice crystal habit on thermal infrared radiative properties and forcing of cirrus. *Journal of Geophysical Research*, **112**, p. D08201.

Wiscombe, W.J., 1977, The delta-M method: rapid yet accurate radiative flux calculations for strongly asymmetric phase functions. *Journal of the Atmospheric Sciences*, **34**, pp. 1408–1422.

Xie, Y., Yang, P., Kattawar, G.W., Baum, B. and Hu, Y.X., 2011, Simulation of the optical properties of ice particle aggregates for application to remote sensing of cirrus clouds. *Applied Optics*, **50**, pp. 1065–1081.

Xie, Y., Yang, P., Kattawar, G.W., Minnis, P. and Hu, Y.X., 2009, Effect of the inhomogeneity of ice crystals on retrieving ice cloud optical thickness and effective particle size. *Journal of Geophysical Research*, **114**, D11203, doi:10.1029/2008JD011216.

Yang, P. and Fu, Q., 2009, Dependence of ice crystal optical properties on particle aspect ratio. *Journal of Quantitative Spectroscopy and Radiative Transfer*, **110**, pp. 1604–1614.

Yang, P., Hong, G., Kattawar, G.W., Minnis, P. and Hu, Y.X., 2008a, Uncertainties associated with the surface texture of ice particles in satellite-based retrieval of cirrus clouds. Part II: effect of particle surface roughness on retrieved cloud optical thickness and effective particle size. *IEEE Transactions on Geoscience and Remote Sensing*, **46**, pp. 1948–1957.

Yang, P., Kattawar, G.W., Hong, G., Minnis, P. and Hu, Y.X., 2008b, Uncertainties associated with the surface texture of ice particles in satellite-based retrieval of cirrus clouds. Part I: single-scattering properties of ice crystals with surface roughness. *IEEE Transactions on Geoscience and Remote Sensing*, **46**, pp. 1940–1947.

Yang, P. and Liou, K.N., 1996a, Finite-difference time domain method for light scattering by small ice crystals in three-dimensional space. *Journal of the Optical Society of America A*, **13**, pp. 2072–2085.

Yang, P. and Liou, K.N., 1996b, Geometric-optics-integral-equation method for light scattering by nonspherical ice crystals. *Applied Optics*, **35**, pp. 6568–6584.

Yang, P. and Liou, K.N., 1997, Light scattering by hexagonal ice crystals: solutions by a ray-by-ray integration algorithm. *Journal of the Optical Society of America A*, **14**, pp. 2278–2289.

Yang, P. and Liou, K.N., 1998, Single scattering properties of complex ice crystals in terrestrial atmosphere. *Contributions to Atmospheric Physics*, **71**, pp. 223–248.

Yuter, S.E., Houze, R.A., Smith, E.A., Wilheit, T.T. and Zipser, E., 2005, Physical characterization of tropical oceanic convection observed in KWAJEX. *Journal of Applied Meteorology and Climatology*, **44**, pp. 385–415.